ChemComm

REVIEW ARTICLE

View Article Online
View Journal | View Issue

Cite this: *Chem. Commun.*, 2026, **62**, 10825

Polysaccharide-based hydrogels and additives in electrolyte engineering for Zn-ion batteries: anode stabilization mechanisms, performance enhancement, and perspectives

Yi Kong,[a] Jicheng Li,[a] Bin-Bin Xie, *[b] Jiele Chen,[a] Hangyi Shen,[a] Hongfei Wang*[a] and Yong Hu *[c]

Aqueous Zn-ion batteries (ZIBs), characterized by intrinsic safety, biocompatibility, and competitive energy density, represent an exceptionally compelling technology for grid-scale energy storage. However, the uncontrollable hydrogen evolution reaction, corrosion, and undesirable dendrite growth triggered by the aqueous electrolytes hamper the further development of ZIBs. In recent years, polysaccharide materials such as cellulose, chitosan, alginates, and cyclodextrins have been widely adopted as electrolyte components in the construction of advanced ZIBs, because of their intrinsically excellent hydrophilicity, environmental friendliness, renewable and abundant production, sufficient active groups, and strong mechanical stability. This review presents a comprehensive summary of the fundamental structures, preparation methods, and comprehensive properties of polysaccharide-based electrolytes. Aqueous ZIBs featuring polysaccharide-based hydrogels are highlighted for their versatile flexibility, high ionic conductivity, and strong adaptability to harsh temperature conditions. To address the active water-derived issues, polysaccharide additives are used to regulate the solvation structures of Zn^{2+} ions and stabilize the anode/electrolyte interface chemistry. Finally, the performance metrics of these strategies are summarized, and the challenges and future perspectives are discussed.

Received 7th April 2026,
Accepted 5th May 2026

DOI: 10.1039/d6cc02122k

rsc.li/chemcomm

[a] *Key Laboratory of the Ministry of Education for Advanced Catalysis Materials, Zhejiang Key Laboratory of Advanced Catalysis and Adsorption Materials, Department of Chemistry, Zhejiang Normal University, Jinhua 321004, China. E-mail: whf0614@zjnu.edu.cn*
[b] *Hangzhou Institute of Advanced Studies, Zhejiang Normal University, Hangzhou 311231, P. R. China. E-mail: binbinxie@zjnu.edu.cn*
[c] *College of Chemistry and Materials Engineering, Zhejiang A&F University, Hangzhou 311300, China. E-mail: yonghu@zafu.edu.cn; Web: https://yonghu.zjnu.edu.cn/*

Bin-Bin Xie

Bin-Bin Xie received his PhD in Chemistry from Beijing Normal University in 2017 under the supervision of Prof. Wei-Hai Fang. He subsequently became an associate professor at Zhejiang Normal University and joined the Chemical Dynamics Team at the Hangzhou Institute of Advanced Studies. His research focuses on the development of nonadiabatic dynamics methods (notably the QTMF program), as well as computational simulations of photochemistry, photobiology and photocatalysis. He also works on molecular dynamics simulations of complex biological systems and machine learning-based approaches to nonadiabatic dynamics.

Hongfei Wang

Hongfei Wang received his PhD degree from the University of Science and Technology of China (USTC) in 2021, and he joined Zhejiang Normal University as an associate professor. His work focuses on the preparation of advanced electrode materials and hydrogel electrolytes in supercapacitors and Zn-ion batteries, as well as the synthesis of catalysts toward the methanol electrooxidation reaction.

1. Introduction

With the rapid depletion of fossil fuels and environmental degradation, there is an urgent need to develop advanced energy storage technologies that are low cost, sustainable, and eco-friendly.[1–7] Over the past decades, Li-ion batteries (LIBs) with high energy density have become the most widely deployed rechargeable batteries.[8–10] Unfortunately, safety concerns and unsustainable Li resources hinder the large-scale deployment of LIBs.[11,12] As some of the most promising alternatives to next-generation batteries, aqueous Zn-ion batteries (ZIBs) have attracted extensive attention due to their abundant Zn resources, intrinsic safety, and high theoretical specific capacity (820 mAh g^{-1} or 5849 mAh cm^{-3}).[13–22] A typical ZIB configuration consists of a cathode, a Zn metal anode, and a glass-fiber separator impregnated with a Zn^{2+}-containing aqueous electrolyte. During charge/discharge cycling, Zn^{2+} ions are reversibly stripped from or electroplated onto the Zn anode, while simultaneously being inserted into or extracted from the cathode material.[23,24]

Among all the constituent components of ZIBs, the electrolyte plays a crucial role in the final electrochemical performance.[25–27] Beyond facilitating ion transport between electrodes, the electrolyte critically determines the electrochemical stability potential window (ESPW), charge/discharge reaction pathways, and the durability of Zn plating/stripping, ultimately governing the cell's tolerance to extreme temperatures. In addition, the choice of electrolyte is also significant for the accurate assessment of electrode materials. To date, the common electrolytes based on $ZnSO_4$, $Zn(ClO_4)_2$, and $Zn(CF_3SO_3)_2$ solutions have been widely adopted due to their excellent compatibility with electrodes. However, the ZIBs using conventional aqueous electrolytes often suffer from attenuated cycling performance and poor Coulombic efficiency (CE), which mainly originate from Zn dendrites, hydrogen evolution reactions (HER),[28] and corrosion at Zn anodes.[29–35] Besides, the demands for flexibility, tough mechanical strength, and leakage avoidance have brought solid-state electrolytes into focus. In this regard, a series of strategies for developing hydrogels or introducing functional additives have been employed to achieve prolonged lifetime and flexibility of ZIBs.[36–39]

Recently, naturally occurring biomass materials, which are easy to obtain and process, have shown great potential in electrolyte systems of ZIBs. Among them, naturally occurring, plant-derived polysaccharides, such as cellulose,[40–44] chitosan,[28,45,46] alginates,[47–50] cyclodextrins,[51] *etc.*, have emerged as promising materials due to their rich polar groups (–OH, $–NH_2$,$–COO^-$, *etc.*). Owing to their high availability, tunable physicochemical properties, and structural diversity, polysaccharides have been extensively investigated in fields ranging from coatings and biomedicine to energy storage.[52–54] In terms of chemical composition, polysaccharides are composed of repeating monosaccharide units, and they can also be assigned positive or negative charges after functionalization. Moreover, the intermolecular and intramolecular hydrogen bonds in the systems can create favorable conditions for further molecular modifications, including grafting, esterification, and etherification.[55,56] The hydrogen bonds among neighboring molecular chains form regular crystalline regions, which contribute to the efficient transport of ions and the construction of hydrogel frameworks with high mechanical strength.[57–60] Accordingly, the unique chemical bonds and functional groups can serve as the transport sites of Zn^{2+} ions and accelerate ionic migration.[61,62] Anions can also interact with polar functional groups to promote the dissociation of electrolyte salts.[63] Indeed, green processes (*e.g.*, moderate temperatures or non-toxic solvents) enable the scalable production of polysaccharides, enhancing their commercial viability.[64–66] Beyond scalability, the intrinsic diversity of polysaccharides, defined by their functional groups, allows them to play various roles in regulating electrolyte behavior.

Compared to commonly used synthetic hydrogel polymers such as polyacrylamide (PAM), polyvinyl alcohol (PVA), and polyethylene oxide (PEO), natural polysaccharides offer several distinctive advantages.[67] Polysaccharides are inherently renewable, biodegradable, and derived from abundant biomass sources, whereas most synthetic polymers rely on petrochemical feedstocks. The extensive hydrogen-bonding networks in polysaccharides allow for excellent mechanical strength and structural stability without sacrificing ionic conductivity, addressing a common trade-off in synthetic hydrogel systems. Moreover, polysaccharides can be processed under mild, environmentally friendly conditions, enhancing their scalability and commercial viability. These inherent features position polysaccharides as unique promising platforms for advanced electrolyte engineering in ZIBs.[68]

Harnessing the unique properties of polysaccharides and capitalizing on recent research advances, this article presents a comprehensive review of polysaccharide-based electrolytes for ZIBs. Given the absence of a systematic summary in this rapidly evolving field, we examine recent studies to elucidate the functional advantages of polysaccharides in aqueous electrolyte

Yong Hu

Yong Hu obtained his PhD degree in inorganic chemistry in 2006 from the University of Science and Technology of China (USTC). He then worked as a research fellow at Nanyang Technological University (NTU). From 2008 to 2024, he worked as a full professor at the College of Chemistry and Life Science, Zhejiang Normal University. In 2024, he joined Zhejiang A&F University as a full professor at the College of Chemistry and Materials Engineering. His current research interests are focused on the design and synthesis of nanomaterials for energy and environmental applications.

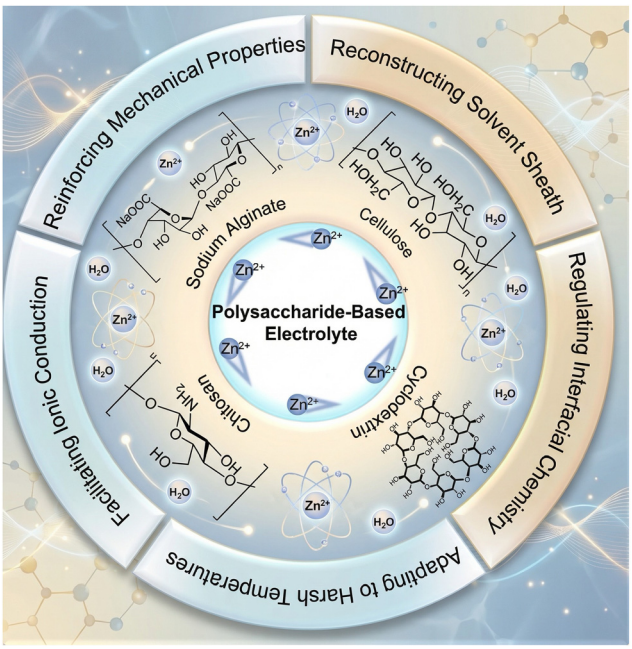

Scheme 1 Several representative polysaccharides for electrolytes of ZIBs.

solutions (Scheme 1). The review first outlines the structural features of key polysaccharides, including cellulose, chitosan, alginates, and cyclodextrins. It then explores their multifaceted roles in electrolyte engineering, specifically in enhancing mechanical integrity, promoting ionic transport, modulating the Zn^{2+} solvation sheath, and stabilizing electrode interfaces. The article concludes with a perspective on the challenges and future directions for developing sustainable, high-performance polysaccharide-based electrolytes for next-generation ZIBs.

2. Fundamentals and challenges of ZIBs

2.1. Interfacial chemistry of Zn anodes in aqueous environments

A typical ZIB consists of a Zn metal anode, an aqueous Zn salt electrolyte, and a cathode.[69,70] Discharge drives the oxidation of Zn to Zn^{2+}, with electrons flowing through the external circuit to the cathode. Charging reverses this process with Zn^{2+} ions extracted from the cathode and plated back onto the Zn anode. This reversible plating/stripping reaction underpins the Zn anode chemistry.[71,72]

The Zn electrodeposition process from the electrolyte onto the conductive electrode substrate can be mainly divided into three steps (Scheme 2a–c). First, the solvated Zn^{2+} ions migrate from the bulk electrolyte to the anode/electrolyte interface under the external electric field.[73] Second, ions diffuse from the outer Helmholtz plane (OHP) to the inner Helmholtz plane (IHP) and are progressively desolvated.[74] Third, Zn^{2+} ions are adsorbed on the surface of the Zn anode, and electrons are transferred from the electrode to the adsorbed cations, allowing the reduction of Zn^{2+} ions to produce Zn metal.[75] Additionally, metal ions may undergo surface self-diffusion at the electrode.[76,77] The migration of charge carriers is known as mass transport, while the other processes belong to charge transfer.[78,79] Generally, the rapid electroplating of Zn^{2+} ions causes ion depletion at the anode/electrolyte interface, resulting in concentration polarization between the electrolyte bulk and the interface. Based on the above analysis, mass transfer depends on the diffusion of hydrated Zn^{2+} ions in the electrolyte.[80] In addition, charge transfer appears at the anode/electrolyte interface, which is governed by the structure of the electric double layer (EDL), the desolvation energy, and the adsorption of cations on the surface.[79,81,82] Reversibly, the Zn metal is stripped to form Zn^{2+} ions during the discharge process (Scheme 2d). Therefore, the electrolyte composition plays a critical role in determining the overall electrochemical performance of ZIBs.

In many electrochemical devices, electrolytes are essential ionic conductors between cathodes and anodes, which offer ionic currents to afford the operation of the cells.[83] In ZIBs, Zn salts are normally dispersed in aqueous solutions to form a primary solvation sheath ($Zn(H_2O)_6^{2+}$), and the corresponding anions also create different solvation structures.[84,85] The properties of aqueous electrolytes, including ionic conductivity, ESPW, Zn^{2+} transference number, *etc.*, are affected by the interactions among Zn^{2+} ions, anions, and water molecules. For Zn salt solutes, the anion species often cause performance differences. Typically, bulky anions possess electron-withdrawing groups that facilitate ionic dissociation and elevate the ion transfer efficiency. Compared with the $ZnSO_4$-containing electrolytes, the $Zn(CF_3SO_3)_2$-based electrolytes exhibit faster transfer kinetics of Zn^{2+} ions and better Zn stripping/plating reversibility.[86,87] The ionic conductivity is related to the viscosity and concentration of electrolytes.[88,89] Normally, with increasing concentration, the ionic conductivity first increases before reaching a peak value and then decreases due to the unfavorable viscosity increase.[86,90] Besides, the anions can alter the pH values and electrochemical reactions of electrolytes.[91–99] For example, active $CF_3SO_3^-$, ClO_4^-, and NO_3^- ions can evolve into solid electrolyte interface (SEI) layers during the repeated charge/discharge processes, thus regulating the interfacial ion diffusion behaviors.[91,92,100] More importantly, the optimized solvation structure in the electrolyte exerts a decisive influence on the Zn conversion reaction at the anode/electrolyte interface.[101] In the pristine electrolyte, the large number of H_2O molecules surround central Zn^{2+} ions to form traditional solvation structures. Based on the modulation of electrolyte engineering, the solvation components undergo structural changes that will affect the interfacial chemistry of the Zn anode.[25,93,99]

2.2. Bottleneck issues caused by aqueous electrolytes

The metallic Zn anode with high theoretical capacity synergizes with the highly conductive aqueous electrolyte, endowing ZIBs with the advantages of high energy density and intrinsic safety. However, there are still some problems to be addressed, such as depletion of active Zn and poor battery lifespan, which are

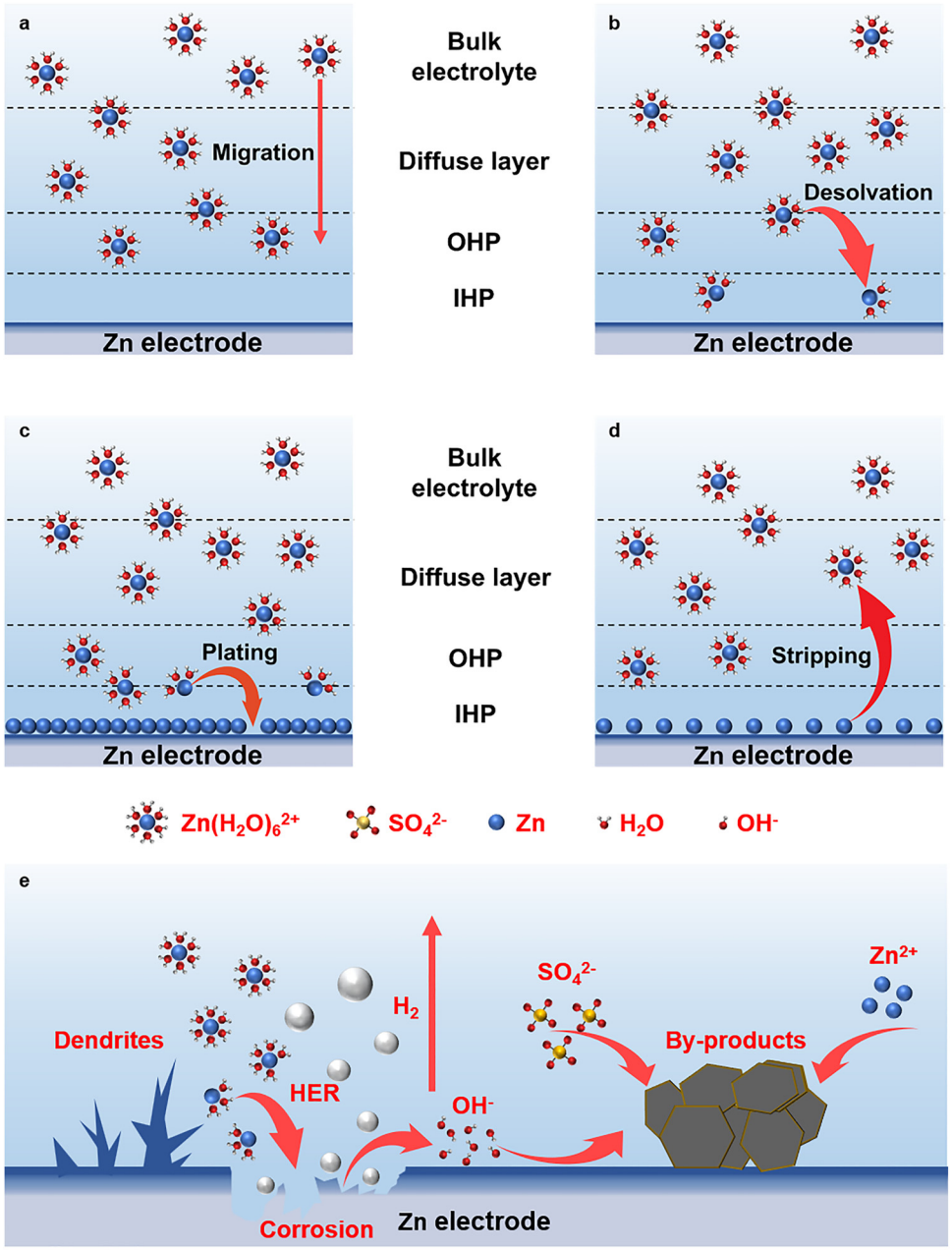

Scheme 2 A schematic representation of the mechanisms of Zn plating and stripping. (a) Migration, (b) desolvation, (c) plating, and (d) stripping. (e) The associated corrosion, passivation, and dendrite growth of the Zn anode caused by aqueous electrolytes.

mainly due to the undesirable interfacial reaction. These interfacial problems consist of the appearance of (1) Zn dendrites, (2) HER, and (3) corrosion (Scheme 2e). These thorny troubles have become the focus of ZIB research.

2.2.1. Zn dendrites. Specifically, Zn dendrites originate from inhomogeneous deposition on locally roughened surfaces of the Zn anode during repeated stripping/plating cycles. Under the driving force of the electric field, Zn^{2+} ions near the anode surface become increasingly concentrated at these protrusions, amplifying the initial surface irregularities and promoting dendritic growth. Upon acquiring electrons from the electrode, Zn^{2+} ions are reduced and deposited at preferential nucleation sites once the nucleation overpotential is exceeded.[102] The surface-adsorbed Zn atoms can diffuse freely and aggregate with other continuously produced Zn atoms at energetically favorable sites on the anode surface, generating a wavy surface topography with multiple small bumps.[103–105] These small bumps are called initial Zn nuclei. After the formation of the initial Zn nuclei, the undesirable surface environment induces inhomogeneous electric fields, which are particularly evident at the tips of the protrusions. Due to the accumulation of surface charges in areas of greater curvature, the intensity of

the electric field in these areas is much stronger than elsewhere,[106–109] which accelerates the growth of dendrites, giving rise to the so-called "tip effect". In addition to tips, the nucleation sites of Zn^{2+} ions also encompass boundaries, dislocation, and impurities.[110] Thus, the evolution of Zn dendrites is fundamentally governed by the inhomogeneity of ionic concentration and electric field distribution, as well as the surface morphology of the Zn anode. These factors are closely associated with electrolyte composition, current density, temperature, and parasitic interfacial reactions occurring at the anode/electrolyte interface.[111]

As dendrites continue to grow, they either eventually penetrate separators or break off into small Zn pieces that are insulated from electrodes, creating "dead Zn".[112] These detached dendrites dispersed within the aqueous electrolyte increase interfacial impedance and reduce anode capacity, while concurrently exacerbating the generation of unfavorable by-products.[113] Worse still, the rampant Zn dendrites offer favorable sites for HER and corrosion due to the loose structure and rough surface.[114]

2.2.2. HER. HER is a critical and serious issue in ZIBs that persists while batteries are resting and running.[94] In conventional Zn salt electrolytes, the reduction of Zn^{2+} ions occurs before HER due to the high HER overpotential and low proton activity. The corresponding reactions are shown in eqn (1) and (2):

$$Zn^{2+} + 2e^- \rightarrow Zn \quad (-0.76\ V) \tag{1}$$

$$2H^+ + 2e^- \rightarrow H_2 \quad (0\ V) \tag{2}$$

In practice, although the rate of HER may be kinetically constrained, HER remains inevitable when the Zn deposition voltage exceeds the ESPW of water. For example, in the commonly used $ZnSO_4$ aqueous electrolyte, the Zn electrodeposition process occurs at a voltage below −0.15 V (*vs.* Zn^{2+}/Zn), which is beyond the thermodynamic stabilization voltage of H_2O (from −0.05 to 1.7 V *vs.* Zn^{2+}/Zn).[115] Moreover, HER is also affected by kinetic factors, including salt concentration,[105] applied current density,[116] operating temperature,[117,118] *etc.* Theoretically, unstable Zn deposition behaviors and non-ideal anode surfaces can also significantly exacerbate HER.

At present, HER severely deteriorates the performance of ZIBs. Irreversible HER competes with Zn deposition for electrons, accompanied by continuous depletion of the electrolyte and active Zn, reducing the batteries' CE and cycling life. The produced hydrogen hinders the Zn nucleation, resulting in large overpotentials and uneven deposition.[119,120] More seriously, the accumulation of hydrogen increases the internal pressure of batteries,[81] leading to expansion and electrolyte leakage,[121] posing a potential risk of fire and explosion. When HER depletes protons near the anode/electrolyte interface, a localized alkaline environment is formed, causing anodic corrosion and electrode passivation.[122]

2.2.3. Corrosion. Electrochemical corrosion of the Zn anode manifests during extended cycling as irreversible active material loss and the accumulation of inert surface by-products.[123] This degradation stems largely from dendrite formation, which exacerbates the morphological instability. Additionally, the oxidation of Zn creates a locally elevated Zn^{2+} concentration near the electrode, drawing anions to the interface and facilitating the precipitation of loose, porous corrosion products ($Zn_4SO_4(OH)_6{\cdot}xH_2O$).[124] In the $ZnSO_4$ electrolyte, the following equations describe the formation mechanism of corrosion products:

$$Zn \leftrightarrow Zn^{2+} + 2e^- \tag{3}$$

$$H_2O \leftrightarrow H^+ + OH^- \tag{4}$$

$$4Zn^{2+} + 6OH^- + SO_4^{2-} + xH_2O \leftrightarrow Zn_4SO_4(OH)_6{\cdot}xH_2O \tag{5}$$

Electrochemical corrosion severely consumes both the electrolyte and Zn reservoir, leading to capacity decay. The accumulation of insoluble by-products reduces the availability of active nucleation sites, resulting in an increasingly inhomogeneous anode surface. Due to the poor conductivity of these corrosion by-products, ion/electron transport is significantly impeded, further elevating the energy barrier for Zn deposition.[125,126] Importantly, these by-products lack the dense, stable structure required to serve as an artificial SEI layer capable of directing uniform Zn^{2+} flux and deposition. Hence, effective interfacial engineering is imperative, not merely to counteract these individual failure modes, but to disrupt their coupled interactions that precipitate rapid battery demise.

3. Fundamental properties of representative polysaccharides

3.1. Cellulose

Cellulose, a linear polymer of D-glucose units linked by β-1,4-glycosidic bonds, is renowned as the most abundant biomass resource on earth (Fig. 1a). Since its first isolation from plants by Anselme Payen in 1838, who also determined its chemical formula, our understanding of this biopolymer has grown significantly. In addition to being a primary structural component of plant cell walls, cellulose is also produced by various microorganisms. It has been the subject of extensive study owing to its abundance of oxygen-containing groups (such as –OH and –OR) and its distinctive molecular structure, which features high porosity and a large specific surface area.[127] These features are key to its function, enabling strong interactions with Zn salts and water molecules.[128,129] This makes cellulose particularly attractive for use in electrolytes. Indeed, its utility is already being realized in ZIBs, where various forms from cellulose nanocrystals to derivatives like bacterial and hydroxyethyl cellulose have shown great promise.[130–134]

The development of green methods for the extraction and dissolution of cellulose is essential for its large-scale utilization.[135] Ionic liquids, such as 1-allyl-3-methylimidazolium chloride and 1-butyl-3-methylimidazolium chloride, represent one such class of effective solvents for this purpose. Another versatile technique is microwave heating, which

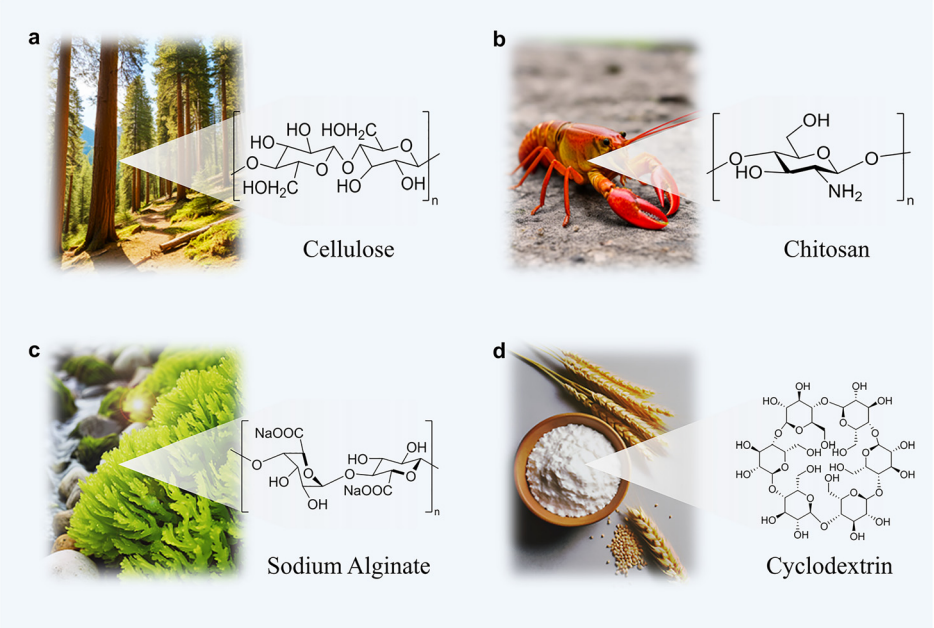

Fig. 1 Structures and natural sources of (a) cellulose, (b) chitosan, (c) sodium alginate, and (d) cyclodextrin.

dramatically expedites the dissolution process and facilitates the separation of cellulose from other woody materials like hemicellulose and lignin. The resulting natural cellulose retains its green credentials, enabling the fabrication of hydrogels without the introduction of toxic substances during electrolyte preparation, thereby enhancing compatibility with other components of ZIBs.[136]

3.2. Chitosan

Chitosan, as the second richest naturally available biopolymer, is a linear cationic polysaccharide material generated by partial deacetylation of chitin.[137] Typically, when the degree of deacetylation exceeds 70%, the resulting product is classified as chitosan. A high deacetylation degree contributes to enhancing the solubility of chitosan in acidic media.[138] Owing to its exceptional physicochemical and biological properties, high-quality chitosan has emerged as a promising candidate for the development of advanced materials across various fields. Recently, the demand for chitosan has continued to rise, prompting researchers to search for new sources of chitin and effective extraction methods. Further exploration of efficient technologies for the conversion of chitin to chitosan has also been emphasized.[139] Chitin itself is a linear biopolymer composed of repeating D-glucosamine and N-acetylglucosamine units and is typically obtained from natural sources (shells of lobsters, crabs, shrimps, *etc.*) *via* biological or chemical processes prior to its conversion to chitosan (Fig. 1b).[140–143]

In fact, modifying the $-NH_2$ groups at the C-2 site and the –OH groups on each monomeric unit is expected to modulate the physicochemical properties of chitosan and further influence the electrochemical performances.[144] In acidic electrolytes, the protonation of H^+ ions in $-NH_2$ allows chitosan to become soluble and offers a more positive charge, which modulates the electrochemical behavior of anions.[141] Essentially, the $-NH_2$ groups in chitosan also exhibit chelating properties to interact with metal ions (Zn^{2+} ions) and further elevate the migration rates. Moreover, the $-NH_2$ and –OH groups can also react with many compounds through carboxylation, acetylation, esterification, alkylation, and hydroxylation reactions, thus enriching the functionality of chitosan.[145]

3.3. Alginates

Alginates are a class of anionic water-soluble polysaccharides derived from brown algae, such as kelp and sargassum.[146] Renowned for their gelling, thickening, and stabilizing properties, alginates are extensively utilized in the pharmaceutical industry. The molecular structure of alginates is formed by mannuronic acid (M) linked to guluronic acid (G) monomers *via* β-1,4-glycosidic bonds.[147] This typical block copolymer comprises alternating longer homopolymerized blocks of both monomers and shorter blocks with sequential monomer distribution. Correspondingly, the distribution, proportion, and length of these blocks affect the final properties of such heteropolysaccharides. The G units are associated with the ability to form gels, while the MM and MG units enhance the flexibility of polymer chains. Besides, the structure of the block copolymer mainly relies on the type and part of the extract. In conventional extraction processes, alginic acid isolated from seaweed is converted into sodium alginate, which is subsequently dissolved, filtered to remove insoluble residues, and recovered. Sodium alginate prepared in this method can produce other alginates like zinc alginate, potassium alginate, and calcium alginate.[148]

The polymer chains of sodium alginate are intrinsically superhydrophilic and ion-exchangeable due to the abundance

of oxygen-containing groups (*e.g.*, –OH and –COONa) and can be easily chemically modified (Fig. 1c).[149–151] Furthermore, sodium alginate-based hybrid materials can be molded into ideal configurations to satisfy practical requirements for energy storage, such as hydrogels, functional groups, and millimeter-sized monoliths.[152–155] For electrolyte applications, the abundant COO^- groups in the backbone enable the preparation of single-ion conductive polymers.[156] Moreover, the GG block is expected to coordinate with Zn^{2+} ions to produce an ''egg box'' composite, thus constructing ion migration channels. Flexible MM and MG blocks also aid in ion transport because their flattened structure offers numerous transport sites for cations.

3.4. Cyclodextrins

Cyclodextrins are a class of polysaccharide products obtained from the enzymatic breakdown of starch.[157] These naturally derived substances fall into the category of caged molecules owing to their stable inner hydrophobic cavities in the center, which allow them to skillfully trap and encapsulate other molecules. This special encapsulation characteristic forms a ''host–guest'' relationship that modifies the physical, chemical, and biological properties of the encapsulated molecules.[158] Currently, there are three types of native cyclodextrins produced on a large scale in a highly purified form, namely α-, β-, and γ-cyclodextrins.[159] Their increasing availability and cost-effectiveness have facilitated widespread applications across diverse fields, including pharmaceuticals, food science, catalysis, and biotechnology.[160–162]

Regarding structural composition, cyclodextrins are described as macrocyclic oligosaccharides comprising 6 to 8 (1,4)-α-D-glucopyranose units. These amphiphilic macromolecules feature relatively hydrophilic surfaces and hydrophobic cavities, which can serve as unique channels for the migration of electrolyte ions on the molecular scale (Fig. 1d).[163] In recent years, it has been reported that the addition of α-, β-, and γ-cyclodextrins in the electrolyte can improve the migration and plating kinetics of Zn^{2+} ions, thus inhibiting the growth of Zn dendrites and improving the cycling stability.[164,165] Mixing cyclodextrins with chain polymers (gelatin, polyacrylic acid (PAA), *etc.*) facilitates the formation of interpenetrating hydrogel networks. These hybrid networks exhibit substantially improved mechanical strength and ion transport properties, rendering them particularly promising for application in quasi-solid-state electrolytes.[166,167]

4. Application of natural polysaccharides in aqueous Zn salt electrolytes

The application of polysaccharides in the electrolytes of ZIBs is mainly carried out in the form of hydrogel frameworks and additive materials. The main motivations behind this research protocol are the low cost of raw materials, reproducibility, and ease of molding, especially for the processing of soluble materials. In addition, the presence of functional groups such as carboxyl and amino groups enriches the function of the electrolytes, yielding superior performance. In the field of Zn-based energy storage, biomass polysaccharide materials have shown superb performance due to their naturally fine structures and plentiful trace elements in organic tissues. The primary experimental parameters to regulate the performance of ZIBs are the physicochemical properties of polysaccharides (molecule size, solubility, zincophilicity, cross-linking, *etc.*). In hydrogels, polysaccharides can be used as reinforcing materials to enhance mechanical properties and stabilize ZIBs under harsh conditions (high/low temperatures, external stress, *etc.*). More importantly, the electrochemical performances of Zn^{2+} ions can be effectively modulated (ionic conductivity, solvation structure, deposition behavior).

4.1. Role of polysaccharides in enhancing the performance of hydrogel electrolytes

4.1.1. Reinforcing mechanical properties. Due to the high Young's modulus and superior stability resulting from high polarity and strong inter/intramolecular hydrogen bonding, some polysaccharides with high crystallinity can be employed as reinforcing materials for hydrogels without sacrificing ion transport properties. One example is the conversion of cotton to cellulose as a polymer framework. After the complete dissolution of cellulose, tetraethyl orthosilicate was introduced and then hydrolyzed to generate $Si(OH)_4$, which can be bonded to the cellulose and pre-incorporated glycerol *via* covalent siloxane bonds, ultimately generating an all-round hydrogel electrolyte. The abundant hydrogen bonds and Si–O–Si bonds can ensure that the hydrogel can withstand deformation (Fig. 2a). High tensile strength (2.11 MPa at the fracture elongation of 846.5%) and elasticity (sustaining $>60\%$ compressive deformation) can be obtained successfully (Fig. 2b). In addition, this hydrogel electrolyte exhibits an ultra-high ionic conductivity of 19.4 mS cm^{-1} at −40 °C compared to other aqueous electrolytes of ZIBs.[40] In another study, carboxymethylcellulose was dispersed within the rigid cellulose to form an interpenetrating double-network hydrogel electrolyte. The NaOH treatment transformed the cellulose I structure into the cellulose II structure. Cellulose I is the native form found in nature, characterized by parallel-oriented polymer chains and a relatively loose packing arrangement. Cellulose II is a thermodynamically more stable polymorph, typically obtained by regenerating or alkali-treating cellulose I, and features antiparallel chain packing with a denser hydrogen-bonding network. This structural transformation from cellulose I to cellulose II is irreversible and generally results in improved mechanical strength due to the more compact and ordered crystalline structure, as well as enhanced chemical stability. Accordingly, the tensile strength is increased from 16 ± 4 MPa to 72 ± 5 MPa.[168] Eventually, the strong mechanical strength contributes to the enhancement of Zn^{2+} conductivity (26 mS cm^{-1}). The repeated charge/discharge tests of ZIBs may cause cyclic loading on the hydrogel electrolyte, which would promote crack initiation and expansion, ultimately leading to hydrogel failure. The fatigue-resistance feature should be emphasized to achieve the long service life

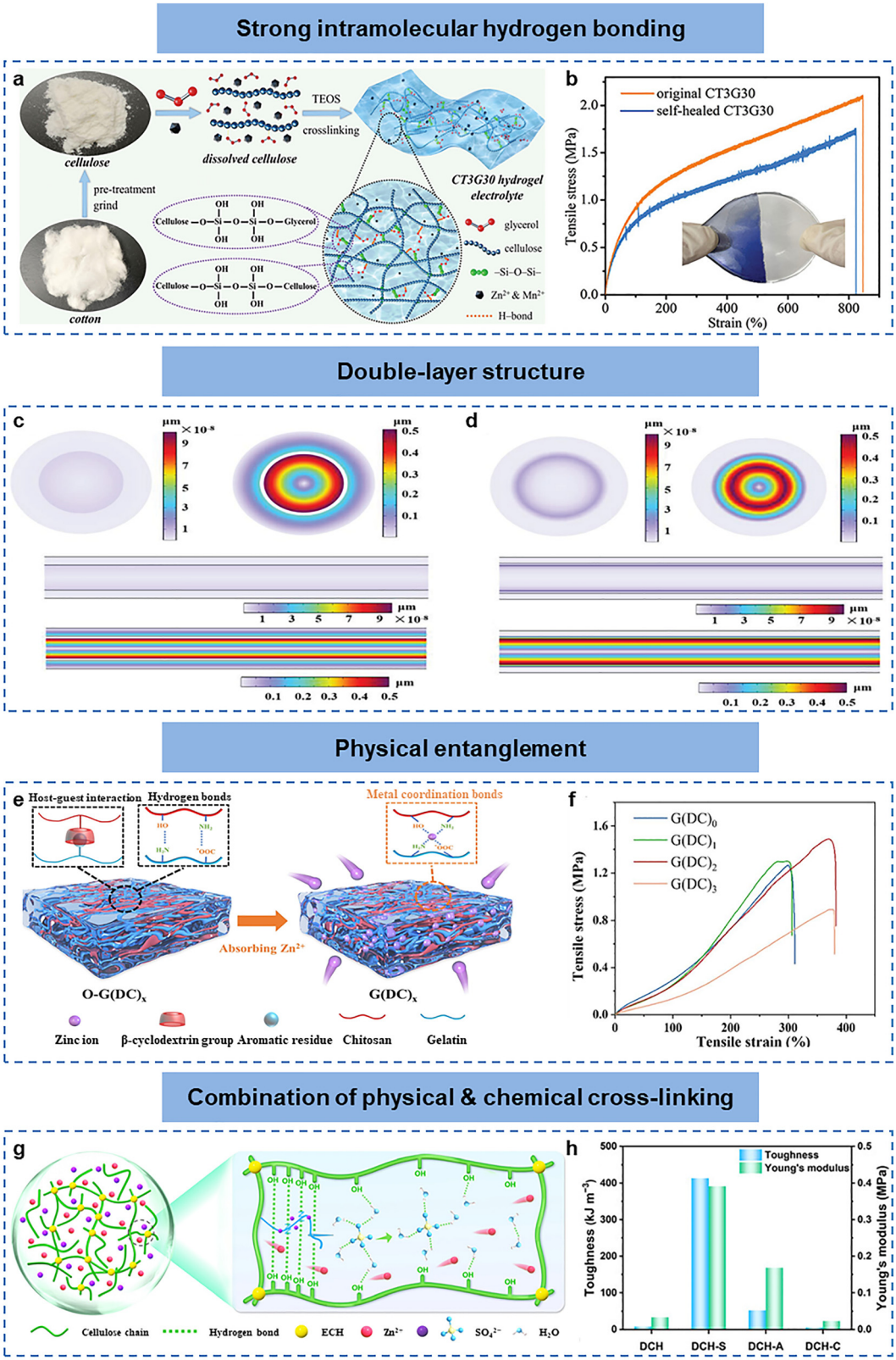

Fig. 2 Methods for strengthening mechanical properties. (a) Synthesis schematic of the cellulose-based hydrogel electrolyte. (b) Tensile σ–ε curves and self-healed performances. Reproduced from ref. 40 with permission from Wiley-VCH, copyright 2021. FES results of (c) the single-layer gel and (d) the dual-layer gel. Reproduced from ref. 174 with permission from Wiley-VCH, copyright 2024. (e) Schematic representation of the $G(DC)_2$ hydrogel electrolyte before and after absorbing Zn^{2+} ions. (f) Tensile curves of different hydrogel electrolytes. Reproduced from ref. 166 with permission from Elsevier, copyright 2024. (g) Schematic diagram of the interactions and Zn^{2+} transport in the DCH-S electrolyte. (h) Toughness and Young's modulus. Reproduced from ref. 181 with permission from Wiley-VCH, copyright 2025.

of batteries. Liu *et al.* incorporated a second polymer of chitosan into the PAM hydrogel electrolyte to yield a $Zn(ClO_4)_2$-PAM-chitosan electrolyte (C-PAMCS). Fourier transform infrared spectroscopy (FTIR) presents the red shift of the N–H stretching peak and the blue shift of the $-NH_2$ in-plane vibration peak for the C-PAMCS network, which should be ascribed to the intermolecular hydrogen bonds formed between PAM and chitosan. Stress–strain curves for continuous compression cycles at 50% strain show no damage to C-PAMCS after 2000 cycles, suggesting that the mechanical stress was effectively dissipated. In this respect, chitosan chains prevent cracks from progressing to the macroscopic level by causing physical entanglement points to slide along the chain or by deforming conformation to effectively absorb the energy generated by compressive stresses. The optimized C-PAMCS delivers a long lifespan of 1500 h for Zn//Zn symmetric cells at 10 mA cm^{-2}/10 mAh cm^{-2}.[45] Also, adding PAA-grafted MXene into PAM/chitosan could fabricate a stable hydrogel electrolyte for ZIBs (MPPC). Ternary hydrogen bonds could be established among chitosan, MXene-grafted-PAA, and PAM. An exceptional mechanical strength of 1.8 MPa could be achieved. The hydrogel-based ZIB shows a maximum capacity of 353 mAh cm^{-3} at 0.5 A cm^{-3} and a long cycling stability of 400 cycles at 2 A cm^{-3}.[169] The design of ionic and covalent crosslinked networks, followed by further processing based on the salting-out effect, improves the mechanical strength of hydrogels. Compounding lignin and chitosan also yields a high-strength hydrogel electrolyte, which possesses superior ductility and tensile strength. The maximum Young's modulus reaches 940 ± 63 MPa, and the largest elongation at break is 43.9 ± 21.1%.[170] Accordingly, a strong hydrogel composed of PVA, sodium alginate, boric acid, and glycerol was developed. Owing to the combined effect of the salting-out effect and energy dissipation mechanism, the hydrogel exhibits robustness and good structural integrity with a tensile strength of 869.4 kPa and an elongation at break of 559.1%.[171] Additionally, the solvent replacement treatment could promote the dissociation of Zn salts and hydrogel network reconstruction. Hence, a sodium alginate/PAM hydrogel was prepared that features a high tensile strength of 61.8 kPa at 310.2%.[60] Besides, the polyanionic hydrogel crosslinked by the induction of Zn^{2+} ions not only guarantees excellent mechanical stability of the electrolyte, but also suppresses the side reactions of the Zn–I_2 battery (I_3^- shuttling, Zn corrosion, HER, *etc.*).[172] This kind of alginate-based hydrogel could also be further incorporated into a typical wire-shaped battery to broaden the application scenarios. Long-time plating/stripping stability, high capacity output, and superior biocompatibility could be achieved.[173]

In the field of flexible ZIBs, Zn dendrites and bending conditions would lead to the interfacial separation of the fibrous electrode from the electrolyte, which severely limits the practical application of devices. In their quest to a ddress the dual challenges of mechanical fragility and dendrite growth in ZIBs, Chen *et al.* engineered a cellulose-based hydrogel electrolyte. The design centers on a Keggin-type polyoxometalate, silicotungstic Zn, which establishes a robust physically crosslinked network. Specifically, the abundant negatively charged oxygen atoms on the silicotungstic acid (STA) surface engage in extraordinarily strong hydrogen bonding and coordination with the hydroxyl groups on cellulose chains. These powerful interactions function as ''molecular rivets'' drawing the loose cellulose chains into a dense and ordered three-dimensional configuration. Consequently, after the incorporation of 2 M $ZnSO_4$, the STA-hydrogel exhibits superior mechanical performance: a tensile strength up to 3.5 MPa, a toughness of 1.5 MJ m^{-3}, and an elongation at break exceeding 80%. This performance surpasses that of most reported pure regenerated cellulose hydrogels, underscoring the effectiveness of STA as a molecular-level reinforcement agent.[128] Li *et al.* developed a bilayer gel electrolyte comprising a fluidic polyvinyl alcohol-Zn acetate inner layer and a robust Zn alginate outer layer *via* a constrained encapsulation strategy to stabilize fibrous Zn anodes. Finite element simulations (FES) reveal that this bilayer design maintains intimate electrode/electrolyte contact during both initial assembly and anode shrinkage, outperforming single-layer structures (Fig. 2c and d). Notably, the gel fills interfacial gaps under severe bending, ensuring structural stability. As a result, the fibrous Zn//Zn symmetric cell operates for 1450 h under static conditions and 800 h under dynamic bending (0.1 Hz) at 1 mA cm^{-2}/1 mAh cm^{-2}. The full cell delivers a capacity of 42.09 mAh cm^{-3} at 0.2 A cm^{-3} with 97.7% capacity retention after 500 bending cycles.[174] Self-healing is a critical requirement for flexible ZIBs to resist mechanical damage. A chitosan/PAM hydrogel electrolyte with a double-crosslinked network was achieved by directly introducing Zn^{2+} ions, eliminating the need for complex post-treatment. The resulting material exhibits a tensile strength of 80 kPa, an ultrahigh elongation at break of 2670%, and load-bearing capacity up to 683 g. The self-healing functionality arises from reversible hydrogen bonds and supramolecular interactions formed *via* Zn^{2+} coordination with amino groups. This intrinsic recoverability guarantees enhanced safety and reliability for flexible ZIBs in practical scenarios.[175] The interfacial stability is critical to facilitating charge transfer and sustaining prolonged charge/discharge processes in flexible batteries. Du *et al.* addressed this by fabricating a PAA-Fe^{3+}-chitosan hydrogel, which was subsequently treated in a $ZnCl_2$/NH_4Cl electrolyte to trigger the precipitation and folding of chitosan micelles *via* the Hofmeister effect. This structural reorganization promotes intimate electrode/hydrogel contact, as evidenced by cross-sectional scanning electron microscopy (SEM). Quantitatively, the interfacial peel strength reaches 1018.7 J m^{-2} when the chitosan content is optimized to 75%, underscoring the effectiveness of this design in enhancing interfacial adhesion.[176]

Physical entanglement between macromolecular chains has also been demonstrated as an effective strategy for enhancing mechanical properties. For instance, a dual-network hydrogel electrolyte composed of PAM and sodium alginate exhibits a maximum tensile strain of 550% and a tensile strength of 15 kPa, both of which are superior to those of pure PAM. This

improvement is primarily attributed to the crosslinking of Zn^{2+} ions with the guluronic acid segments along the sodium alginate chains.[177] Crosslinking chitosan with κ-carrageenan produces a hybrid hydrogel electrolyte (CarraChi) with significantly improved mechanical integrity. The dense network of electrostatic interactions and hydrogen bonds between the two polysaccharides contributes to a tensile strength of 14.2 MPa and an elongation at break of 45%, outperforming both pure κ-carrageenan hydrogel (4.2 MPa, 32%) and commercial glass fiber separators (0.3 MPa, 6%). This enhanced mechanical robustness not only provides a physical barrier against dendrite penetration but also accommodates the volume fluctuations of electrodes during Zn^{2+} insertion/extraction cycles, thereby promoting long-term cycling stability.[178] Impressively, a pouch Zn//Zn symmetric cell with the CarraChi electrolyte shows a long Zn plating/stripping life of ~4000 h at 10 mA cm^{-2}/35 mAh cm^{-2}. Chen *et al.* designed a dual-functional PAZ-S hydrogel electrolyte by integrating sodium alginate, Zn^{2+} ions, and poly(Zn acrylate) (PAZ) into an interpenetrating network. The architecture is formed *via* sequential Zn^{2+} crosslinking of alginate and *in situ* polymerization of Zn acrylate. This design yields a mechanically robust electrolyte with a tensile strength of 3.04 MPa, a modulus of 30.5 MPa, and a toughness of 948.1 kJ m^{-3}, far surpassing those of the pristine SA hydrogel (0.37 MPa, 0.33 MPa, and 423.7 kJ m^{-3}). The PAZ-S electrolyte simultaneously stabilizes the Zn anode and facilitates Mn^{2+} deposition at the cathode. As a result, the Zn/PAZ-S/MnO_2 full cell exhibits excellent rate performance (*e.g.*, 365.8 mAh g^{-1} at 0.2 A g^{-1} and 153.3 mAh g^{-1} at 2.0 A g^{-1}) and prolonged cycling stability, retaining 153.4 mAh g^{-1} (77.2%) after 400 cycles at 0.5 A g^{-1}.[179] Following this idea, a gelatin-based (G) hydrogel electrolyte enriched with chitosan (C) grafted with β-cyclodextrin (D) was designed ($G(DC)_x$, *x* denotes different concentrations of DC; Fig. 2e). The addition of chitosan also increases the content of amino and hydroxyl groups, which builds up the host–guest interactions and enhances the hydrogel network. Indeed, the pure gelatin hydrogel displays a tensile strain of only 97.9% and a low tensile strength of 16.7 kPa. In contrast, the stress–strain curves demonstrate that the $G(DC)_2$ hydrogel electrolyte has a significant improvement in stretchability (1.49 MPa, 400%) when the concentration of DC is 2 wt% (Fig. 2f). This is due to the formation of coordination bonds between Zn^{2+} ions and functional groups on the gelatin and DC chains. As a result, the assembled Zn//Zn symmetric cells using the $G(DC)_2$ electrolyte deliver excellent cycling stability for over 1200 h at 1 mA cm^{-2}/1 mAh cm^{-2}, indicating effective suppression of dendrites.[166]

To synergistically enhance mechanical and transport properties, Zhang *et al.* designed a double-crosslinked cellulose hydrogel (DCZ-gel) integrating chemical and physical crosslinking. The chemical network is formed *via* covalent ether bonds between cellulose hydroxyls and epichlorohydrin, as evidenced by the C–O–C stretching vibration at 1169 cm^{-1}. Superimposed on this is a physical network arising from hydrogen bonding and the formation of cellulose II microcrystalline hydrates in an alcohol–water medium. These physical crosslinks not only reinforce the matrix but also induce phase separation, creating interconnected ion transport channels across nano- to microscales. This hierarchical design achieves an optimal balance of mechanical robustness (tensile strength: 2.08 MPa; elongation: 145%) and ion transport kinetics (ionic conductivity: 38.6 mS cm^{-1}; Zn^{2+} transference number: 0.73). The DCZ-gel thus affords exceptional cycling stability in both symmetric Zn//Zn cells (>400 h at 10 mA cm^{-2}) and Zn//polyaniline full cells (>2000 cycles at 2000 mA g^{-1}).[180] Building on the dual-crosslinking concept with epichlorohydrin (Fig. 2g), researchers have introduced a dimension to hydrogel electrolyte design by systematically leveraging the Hofmeister salt-dissolving effect. This strategy modulates the hydrogen-bonding network within cellulose hydrogels through anion-mediated regulation of water molecule states. Comparative studies reveal that SO_4^{2-} outperforms Ac^- and Cl^- in both salting-in strength and hydrogen-bond regulation capability. The optimized DCH-S electrolyte accordingly exhibits superior mechanical properties: toughness of 413.61 kJ m^{-3}, Young's modulus of 0.39 MPa, and dramatic increases in tensile strength (20.6-fold) and compressive strength (14.0-fold). Simultaneously, it achieves high ionic conductivity (24.1 mS cm^{-1}) and an exceptional Zn^{2+} transference number (0.87) (Fig. 2h). By establishing a direct link between Hofmeister anion selection and electrolyte performance, this work offers a paradigm for designing high-performance flexible ZIBs and highlights the promise of biodegradable materials for sustainable energy storage.[181] In addition, Cao *et al.* reported a cellulose nanofibril-based morphing gel electrolyte (MorphGE) with favorable mechanoadaptive performance. Massive cellulose nanofibrils were assembled into MorphGE in a layer-by-layer stacking fashion, endowing it with a high modulus of ~ 1.48 MPa. The maximum elongation and tensile strength could reach 128% and 3.22 MPa, respectively. Moreover, the material possesses a long plastic deformation stage between 2% and 41%, which is also strong evidence that MorphGE is deformable. These performances contribute to stabilizing the electrochemical reactions at the gel–electrode interface and directing the homoepitaxial uniform Zn deposition with a hexagonal structure.[182]

In summary, the mechanical robustness of polysaccharide-based hydrogel electrolytes is governed by several design principles. First, the introduction of covalent crosslinking (*e.g.*, *via* epichlorohydrin or siloxane bonds) and physical crosslinking (*e.g.*, hydrogen bonding, ionic coordination, and chain entanglement) synergistically enhances tensile strength and toughness. For instance, cellulose-based hydrogels have achieved tensile strengths exceeding 2 MPa and ionic conductivities above 38 mS cm^{-1}. Second, the salting-out effect and Hofmeister anion regulation have been shown to dramatically improve the Young's modulus and compressive strength by modulating hydrogen-bonding networks. Third, double-network and interpenetrating network architectures, combining rigid polysaccharides (*e.g.*, cellulose, chitosan) with ductile synthetic polymers (*e.g.*, PAM, PVA), offer an effective strategy to balance strength and flexibility. Notably, hydrogels with tensile

strengths in the range of 0.5–3.5 MPa and elongations exceeding 400% have been successfully developed, enabling stable cycling over hundreds to thousands of hours under high current densities. Such mechanical integrity not only physically suppresses Zn dendrite penetration but also accommodates volume fluctuations during repeated plating/stripping, thereby prolonging battery lifespan. Future efforts should focus on further improving fatigue resistance and self-healing capabilities while maintaining high ionic conductivity, especially for practical flexible and wearable applications.

4.1.2. Facilitating ionic conduction. Owing to their abundance of polar functional groups and their ability to form well-defined architectures, polysaccharides offer a promising platform for fabricating ion-conductive hydrogel electrolytes. The microporous networks derived from these materials play a key role in stabilizing the ionic transport channels, thereby supporting efficient and reliable ion conduction.[183] Shi *et al.* utilized eutectic Ga–In (EGaIn) microdroplets to initiate acrylamide polymerization, producing a PAM-hemicellulose/EGaIn composite hydrogel that was subsequently 3D-printed into freestanding scaffolds. The resulting network integrates covalent and hydrogen bonds, enabling uniform stress distribution and Zn^{2+} flux homogenization as confirmed by FES (Fig. 3a and b). Electrochemical impedance spectroscopy (EIS) demonstrates that this Zn-affinitive hydrogel reduces charge transfer resistance in Zn//Zn symmetric cells, minimizing polarization during Zn electrodeposition.[41] In another example, an amphoteric carboxylethyl cellulose-based hydrogel electrolyte was fabricated (PCZ-gel) (Fig. 3c). The amphoteric groups on the polymer chains including carboxyl and quaternary ammonium contributed to the dissociation of $ZnSO_4$ salt, thus elevating the ionic conductivity from 23.9 mS cm^{-1} (pure PAM hydrogel) to 27.5 mS cm^{-1} (PCZ-gel). Particularly, the concentration polarization at the Zn anode/electrolyte interface could be further alleviated, and the Zn^{2+} transference number of PCZ-gel (0.72) is higher than that of the liquid electrolyte (0.43).[184] Analogously, a multi-component cross-linked hydrogel electrolyte denoted as PCA was synthesized *via* heat-initiated polymerization of three components (PAM, carboxymethyl cellulose (CMC) and agarose (AG)). Owing to the physical entanglement and hydrogen bond cross-linking among the three components, a three-dimensional network structure was formed. The PCA hydrogel electrolyte exhibits a high ionic conductivity of 38.78 mS cm^{-1} and excellent mechanical strength from 2.9 MPa to 5.6 MPa. Therefore, the hydrogel electrolyte enables both exceptional cycling stability in a Zn//Zn symmetrical cell for over 2500 h (1 mA cm^{-2}) and a remarkable capacity retention of 97.8% in a Zn//MnO_2/CNT full cell, retaining 127.2 mAh g^{-1} after 1000 cycles at 1 A g^{-1}.[185] Wang *et al.* developed a gradient-network hydrogel electrolyte composed of PVA, cellulose nanofibers (CNF), and graphene oxide (GO), which is denoted as PCG (Fig. 3d). The polar oxygen-containing groups (OH, –COOH) enriched in PVA, CNF and GO preferentially coordinate with Zn^{2+} with a higher binding energy (PVA: −10.70 eV, CNF: −12.32 eV, GO: −12.91 eV) than water molecules (−4.73 eV), effectively weakening the hydration shell of Zn^{2+} and reducing the desolvation activation energy (Fig. 3e). At the microscopic structure scale, the high-density PCG layer facing the negative electrode uniformly distributes the ion flux and ensures uniform electric field distribution, inhibiting dendrite nucleation and with a nucleation overpotential of only 49 mV, while the low-density PC layer (without GO), with a pore size of 15–40 μm, facing the positive electrode ensures high ionic conductivity (up to 16.18 mS cm^{-1}). The introduction of GO enhances the Zn^{2+} migration number to 0.45, its dielectric properties further promote ion transport, and its hydrophilic network binds water molecules, reducing the corrosion current density to 0.27 mA cm^{-2}, thereby achieving a synergistic effect of rapid ion transport, uniform dendrite-free deposition and efficient inhibition of side reactions simultaneously.[186] More impressively, a nano-engineered functional solid-state electrolyte containing Zn^{2+}-coordinated carboxylate cellulose nanofibers (CCNF) and xanthan gum (Zn-CCNF@XG) for ZIBs was also constructed to form favorable Zn^{2+} hopping sites. The molecular electrostatic potential (MESP) distribution reveals that the negative charge centers are mainly concentrated on the hydroxyl, carboxyl, and ether bonds, which could act as Zn^{2+} hopping sites. Molecular dynamics (MD) simulations further reveal that Zn^{2+} ions rapidly migrate along the CCNF chains, while the CCNF backbones remain nearly stationary, indicating that the Zn^{2+} ions are dissociated from the polymer chains. Specifically, density functional theory (DFT) calculations demonstrate that carboxyl functional groups are beneficial for decreasing the dissociation energy (Fig. 3f–h), which is responsible for Zn^{2+} decoordinating and fast ion-hopping. Consequently, the ionic conductivity and Zn^{2+} transference number are as high as 1.17×10^{-4} S cm^{-1} and 0.78, respectively. Benefiting from the engineered molecular channels, the Zn//Zn asymmetric cell based on Zn-CCNF@XG displays a long plating/stripping CE of 99.51% over 1000 cycles at 0.5 mA cm^{-2}/0.5 mAh cm^{-2}, and the Zn//Zn symmetric cell could run for 3600 h with a small overpotential value of 40 mV. Moreover, the Zn//$NaV_3O_8 \cdot 1.5H_2O$ full battery equipped with Zn-CCNF@XG could retain 83.46% of initial capacity after 3000 cycles at 1 A g^{-1}.[187]

Currently, low Zn utilization and retarded ionic diffusion cause severe parasitic side reactions, which greatly hinder the application of ZIBs. In this respect, Zhang *et al.* reported an innovative chitosan-based gel/solid synergistic electrolyte to improve Zn utilization and prolong cycling life. A protonated chitosan hydrogel layer was first constructed at the electrode interface, serving as a diffusion layer. Concurrently, a solid electrolyte film forms on the Zn anode surface *via* ionic complexation between Zn^{2+} ions and chitosan chains, yielding a dense Zn/chitosan polymer layer. The elevated Zn^{2+} concentration at the hydrogel/anode interface accelerates ionic diffusion within the diffusion layer and enables dendrite-free Zn deposition. Specifically, the protonated chitosan electrolyte at an optimal concentration of 2% achieves a high ionic conductivity of 2.4 μS cm^{-1} and effectively reduces concentration polarization.[188] To enhance interfacial stability and cycling performance, a hybrid gel electrolyte comprising chitosan and

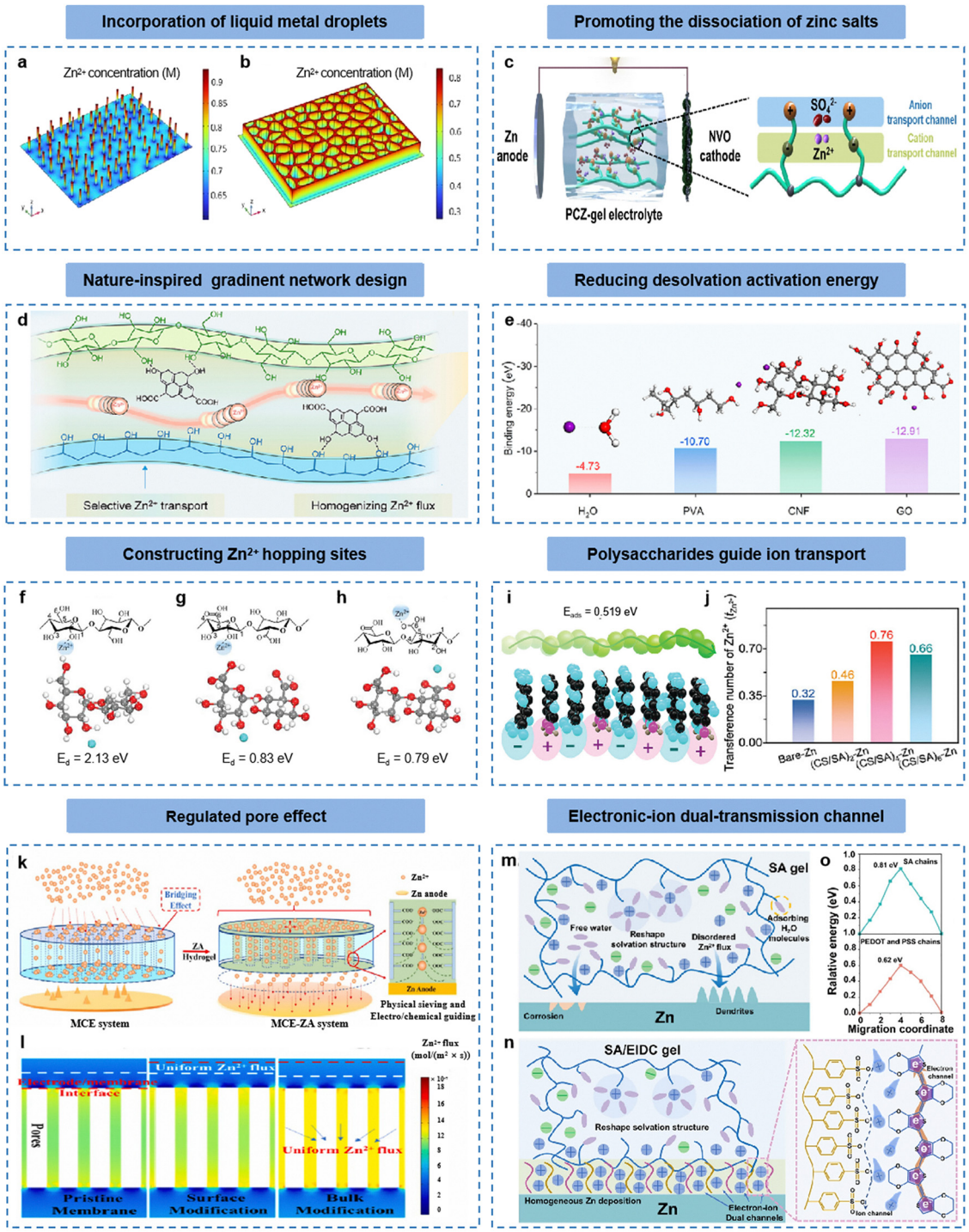

Fig. 3 Methods for facilitating ionic conduction. Simulation of the Zn^{2+} concentration distribution for (a) the Zn foil and (b) the modified electrode. Reproduced from ref. 41 with permission from Wiley-VCH, copyright 2023. (c) Schematic diagram of the battery using a PCZ-gel electrolyte. Reproduced from ref. 184 with permission from Wiley-VCH, copyright 2023. (d) Schematic illustration of the ''cartilage-inspired'' gradient-networked hydrogel electrolyte. (e) The DFT calculations for the binding energies of Zn^{2+} to PVA, CNF, and GO molecules. Reproduced from ref. 186 with permission from American Chemical Society, copyright 2025. Dissociation energies of Zn^{2+} with –OH on C_2 of (f) CNF, (g) CCNF, and (h) –COOH of CCNF. Reproduced from ref. 187 with permission from Wiley-VCH, copyright 2024. (i) DFT calculated Zn^{2+} transport path. (j) Comparison of Zn^{2+} transference numbers. Reproduced from ref. 48 with permission from Wiley-VCH, copyright 2023. (k) Schematic illustration of the zinc alginate hydrogel electrolyte membrane system. (l) The Zn^{2+} field models of different membranes. Reproduced from ref. 195 with permission from Elsevier, copyright 2024. Schematic illustrations of Zn anodes in a (m) SA gel electrolyte and (n) SA/EIDC gel electrolyte. (o) The comparison of migration energy barriers in the SA gel layer and EIDC polymer layer. Reproduced from ref. 197 with permission from Elsevier, copyright 2025.

Zn-MOF-74 was designed with a hierarchical porous architecture. The chitosan matrix, formed through acid dissolution and alkaline coagulation, provides micron-scale pores, while the incorporated MOF contributes nano-scale porosity, collectively facilitating ion transport. The abundant hydroxyl and amine groups on chitosan chains promote intimate contact with the Zn anode surface, ensuring uniform Zn plating/stripping and reducing the deposition overpotential to ≈155 mV at 50 μA cm^{-2}, compared to ≈280 mV in conventional systems.[189] Recognizing that the ionic conductivity of hydrogel electrolytes is intrinsically linked to their polymer structure and functional groups, Hu *et al.* designed a sulfonated chitosan hydrogel (SCS) by grafting sulfonate groups onto chitosan and crosslinking with PAM. The incorporated sulfonate groups enhance ion transport, yielding a superior ionic conductivity of 38.1 mS cm^{-1}, markedly higher than that of unmodified chitosan (28.2 mS cm^{-1}). This conductivity enhancement supports prolonged Zn//Zn symmetric cell operation exceeding 2600 h at 1 mA cm^{-2}/1 mAh cm^{-2}. Full batteries leveraging the SCS electrolyte further demonstrate excellent rate capability (394.5 mAh g^{-1} at 0.1 A g^{-1}) and cycling stability (96.1% retention after 500 cycles at 1 A g^{-1}).[190] Harnessing intermolecular forces such as van der Waals interactions, electrostatics, and hydrogen bonding, a layer-by-layer self-assembled gel electrolyte was constructed using two oppositely charged natural polysaccharides: sodium alginate and chitosan. The alternating charge distribution within the multilayered structure creates a favorable pathway for Zn^{2+} migration, as evidenced by a DFT-calculated diffusion energy barrier of 0.519 eV (Fig. 3i). Electrochemical characterization further confirms that the four-layer stacked configuration promotes efficient ion transport, achieving a Zn^{2+} transference number of 0.76 (Fig. 3j).[48] Adding a chlorophyll derivative into the chitosan-based hydrogel network was reported to construct ternary hydrogen bonds. The multipolar groups introduced by this modification enable effective redistribution of Zn^{2+} ions and guide their preferential deposition along the Zn (002) plane. This structural regulation translates into enhanced ion transport, as evidenced by an ionic conductivity of 3.6 mS cm^{-1} and a Zn^{2+} transference number of 0.6.[191] The combination of MXenes with the chitosan chain was proposed to reduce the Zn^{2+} ion gradient at the anode interface, homogenize the ionic flux, and avoid polarization.[192] Similarly, the introduction of chitosan into the PVA network delivered the same effect.[28] The chitosan hydrogel could also be prepared by first immersing in the Zn^{2+}-saturated NaOH solution and then draining extra water. The water content was reduced by confining the aqueous electrolyte within micropores, thereby increasing the ionic conductivity to 72 mS cm^{-1}.[193] The functionalized chitosan (carboxymethyl chitosan) interacted with Zn^{2+} ions by virtue of monodentate carboxyl, hydroxyl, and amino groups. This hydrogel electrolyte acts as a flexible medium to boost electrochemical kinetics.[194]

Zn alginate belongs to the class of hydrogel electrolytes with high ionic conductivity, typically in the range of 1.8–3.3 × 10^{-2} S cm^{-1}. Its structure is rich in zincophilic carboxyl and ether groups, which can direct the ordered diffusion of Zn^{2+} ions and effectively suppress parasitic side reactions. As a demonstration, a Zn alginate hydrogel was prepared *via in situ* crosslinking conversion of sodium alginate and subsequently employed as a Zn^{2+} redistributor at the anode interface. Following desolvation, Zn^{2+} ions tend to migrate in a ''Z-type'' pathway along the nearest carboxyl groups within the alginate network. DFT calculations reveal a low migration barrier of 0.70 eV for this ''Z-type'' transport, indicating a shortened diffusion distance and accelerated migration kinetics. Concurrently, free SO_4^{2-} anions are effectively repelled, yielding a high Zn^{2+} transference number of 0.82.[61] To address the challenges of dendrite growth and interfacial instability, Yan *et al.* designed a porous membrane functionalized with *in situ* crosslinked Zn alginate hydrogels, creating continuous and stable ion transport channels (Fig. 3k). The well-defined pore structure works in concert with the zincophilic carboxyl/ether groups of Zn alginate to reduce the energy barrier for transmembrane Zn^{2+} migration. Furthermore, this architecture promotes a uniform surface electric field distribution, effectively suppressing Zn dendrite formation and mitigating parasitic side reactions at the electrode/electrolyte interface (Fig. 3l).[195] In addition, Zn alginate as a filler was also incorporated into a thermoplastic polyurethane fiber matrix. Zn^{2+} ions were confined in the alginate network to construct an egg-shell structure. The integration of Zn alginate and thermoplastic polyurethane results in an ionic conductivity of 16.4 mS cm^{-1}, higher than that of the liquid electrolyte (13.4 mS cm^{-1}). The Zn plating/stripping cycling stability reaches 1200 h at 5 mA cm^{-2} and 5 mAh cm^{-2}. The cumulative capacity is over 6000 mAh cm^{-2}. The full battery coupled with a V-based cathode delivers a capacity of 476 mAh g^{-1} at 0.5 A g^{-1}, and long-term cyclic stability with a capacity retention of 68.6% at 10 A g^{-1} could be achieved.[196] Moreover, an anionic polyelectrolyte based on sodium alginate was deployed to regulate the migration and deposition behaviors of Zn^{2+} ions. The unique electrostatic interaction of Zn^{2+} ions with alginates *in situ* induced an accelerated channel with an ordered porous structure. The Zn^{2+} transference number could be effectively increased to 0.437. DFT calculations also confirmed that the (002) plane is the mainly exposed plane with the adjustment of sodium alginate. The *in situ* Raman demonstrates that this hydrogel electrolyte could ensure reversible plating/stripping processes according to the periodic $-COO^-$ intensity variation. Under a high depth of discharge (DOD) of 57.1% (10 mA cm^{-2}/10 mAh cm^{-2}) with a Zn foil thickness of 30 μm, the Zn//Zn symmetric cell could maintain a stable operation of 140 h with a small potential difference of 0.114 V. The Zn//MnO_2 full battery shows the largest specific capacity of around 280 mAh g^{-1} at 0.1 A g^{-1} and holds a capacity retention of 87.1% for 3000 cycles at 5 A g^{-1}.[44] The sodium alginate hydrogel was also used as the main base for constructing hydrogel electrolytes. Wang *et al.* constructed an electronic-ion dual-transmission channel polymer layer (EIDC) composed of poly(3,4-ethylenedioxythiophene) (PEDOT) and polystyrene sulfonate (PSS) on the surface of the sodium alginate gel. Inside

the sodium alginate gel network, the polymer chains weaken the interaction between Zn^{2+} and water molecules, restructuring the Zn^{2+} solvation sheath. Meanwhile, the $-SO_3^-$ groups in the electron-ion dual-conductive (EIDC) polymer layer create a uniform and efficient pathway for Zn^{2+} transport *via* electrostatic interactions. Concurrently, conjugated π–π bonds along the PEDOT chains form continuous electron-transport channels, accelerating charge transfer during Zn deposition/dissolution. Zn^{2+} primarily migrates along pathways defined by the most closely positioned carboxylate ($-COO^-$) groups, as depicted in Fig. 3m. Regarding transport within the PEDOT:PSS composite matrix, it illustrates that Zn^{2+} preferentially moves *via* pathways coordinated by –OH and $-SO_3^-$ functional groups (Fig. 3n). This route presents a lower migration energy barrier of 0.62 eV, in contrast to the higher barrier of 0.81 eV observed for diffusion through the sodium alginate network alone (Fig. 3o).[197] Another SiO_2-enhanced sodium alginate hydrogel was devised to modulate the solid–liquid interaction energy and the material distribution in the EDL. MD simulations substantiate that the unfavorable free water molecules and SO_4^{2-} anions could be expelled from the EDL due to abundant $-COO^-$ groups, which benefits rapid Zn^{2+} transport kinetics (Zn^{2+} transference number: 0.710) for stable Zn deposition. FES further indicates that Zn^{2+} flux can be homogenized and dendrite-free reactions can be achieved with the aid of this hydrogel. The protective layer could endow the Zn//Zn symmetric cells with a long cycling stability of 3000 h at 2 mA cm^{-2}/1 mAh cm^{-2}. The high-loading ZIB (6.5 mg cm^{-2}) exhibits a high capacity of 2.05 mAh cm^{-2} and only 11.85% capacity attenuation for 1500 cycles.[198] Also, the cross-linking of sodium alginate and tannic acid modulates the coordination structure of Zn^{2+} ions and enhances ionic conductivity.[199] Lin *et al.* reported the integration of alginate and graphene oxide to form a dual-functional hydrogel. The shuttling effect of polybromide could be suppressed by the negatively charged groups, and the Zn^{2+} transport was boosted to restrain corrosion.[200] In another sample, Zn alginate and conductive acetylene black were mixed to produce an electronic–ionic mixed layer. An effective channel was created in which the migration of Zn^{2+} ions was guided by the carboxylate groups.[201] The addition of vermiculite sheets into Zn alginate could offer a Zn^{2+} migration channel, elevating the Zn^{2+} transference number to 0.81. The symmetric cell delivers a long cycling stability of 1000 h at 2 mA cm^{-2}/1 mAh cm^{-2}.[202]

Considering the difficulty of moving divalent ions in the polymer system, relying solely on the effect of anions grafted onto the hydrogel chains to achieve single Zn^{2+} transport is not ideal. Water molecules are good media for transporting both cations and anions, allowing aqueous electrolytes to be typical binary ionic conductors. Fortunately, solvent water molecules can be confined to the hydrophilic network of the hydrogel matrix. Cyclodextrins with ring-shaped molecular structures can coordinate with polymer chains to guide the directional movement of Zn^{2+} ions. Xia *et al.* developed a hydrogel electrolyte with a single Zn^{2+} conducting property by integrating PAM and pseudo-polyrotaxane structure. Such a special pseudo-polyrotaxane structure consists of linear PEO and α-cyclodextrins that could slide along the polymer chains. Based on the spatially steric effect, the OTf^- anions can be locked between two cyclodextrin molecule rings, while Zn^{2+} ions are directed to migrate under the guidance of the abundant hydroxyl sites on the outside of the rings. MD simulation was performed to elucidate the transport mechanisms of Zn^{2+} ions in the cyclodextrin-PEO/PAM hydrogel electrolyte. The hydrated Zn^{2+} ion clusters migrated along the PEO chains when an external electric field was exerted along the chain direction. This motion law could be further evidenced by the change in the internal energy curve. In the MD simulation, the energy profile of Zn^{2+} migration along the polymer chain exhibits three distinct plateaus (plateau I, II, and III), each corresponding to temporary localization of hydrated Zn^{2+} ions at specific interaction sites. Plateau I represents the initial binding event, where Zn^{2+} ions are captured by the first α-cyclodextrin ring *via* hydrogen bonding between the hydrated ion and the hydroxyl groups on the cyclodextrin exterior. Plateau II reflects a metastable state as the ion moves toward an adjacent cyclodextrin unit, involving partial desolvation and re-coordination with ether oxygen atoms from the polyethylene oxide chain threaded through the cyclodextrin cavity. Plateau III corresponds to the final stabilization step, where the ion becomes fully accommodated within the next cyclodextrin ring or at the interface between two cyclodextrin units. During the plateau I phase, a distinct energy-stabilizing plateau could be observed, indicating that hydrated Zn^{2+} ions were temporarily localized at α-cyclodextrins. Similar plateau II and plateau III also emerged. Accordingly, an ultrahigh Zn^{2+} transference number of 0.923 and a large ionic conductivity of 22.4 mS cm^{-1} could be successfully realized. The Zn//Zn symmetric cell demonstrated a stable Zn plating/stripping process for more than 160 h. The ZIB with a La^{3+} doped V_2O_5 cathode could offer a high capacity of 439 mAh g^{-1} at 0.1 A g^{-1} and exhibit a capacity retention of 90.2% for 3500 cycles at 5 A g^{-1}.[203] Similarly, Cai *et al.* used gelatin (G) as the basic network and introduced β-cyclodextrin grafted chitosan (DC) as the functional component, which integrated the advantages of β-cyclodextrin and chitosan. The hydrophobic cavity of β-cyclodextrin formed host–guest interactions with aromatic amino acids (tyrosine, tryptophan, phenylalanine) in gelatin, strengthening the hydrogel structure, and the abundant $-NH_2$ and –OH groups from the chitosan formed coordination bonds with Zn^{2+}, guiding uniform ion flux and deposition. As a result, the $G(DC)_2$ hydrogel electrolyte exhibits a high ionic conductivity of 24.89 mS cm^{-1} and an elevated Zn^{2+} transference number of 0.49, outperforming other hydrogel electrolytes and enabling efficient Zn^{2+} transport.[166] In another work, a cyclodextrin-based polymer (CD-Si) was prepared by a nucleophilic substitution reaction. Embedding CD-Si in the PEO and polyvinylidene fluoride (PVDF) matrix could form a solid polymer electrolyte (SPE). The PEO chains as guest molecules were interspersed in the cavity of CD-Si rings as host molecules, thus constructing non-covalent ion transmission channels. Differential scanning calorimetric (DSC) curves reveal that the glass transition

temperature (T_g) of PEO/PVDF/CD-Si (56 °C) is higher than that of PEO/PVDF (30 °C) and PEO/PVDF/CD (48 °C). This suggests that the incorporation of CD-Si improves the motility of polymer matrices and reduces their crystallinity. MD simulation clearly shows that the addition of CD-Si results in a more homogeneous distribution of PEO and PVDF. In the presence of CD-Si, Zn^{2+} ions are liberated from pristine compact structures with reduced coordination and enhanced migration. The ionic conductivity and Zn^{2+} transference number could reach 1.64×10^3 S cm^{-1} and 0.67, respectively, which is mainly ascribed to the non-covalent anchoring of CD-Si.[164] Inspired by the nano-drug delivery, a gel polymer electrolyte was developed by the self-assembly of PEO and α-cyclodextrin. By virtue of abundant hydrogen bonds, Zn^{2+} ions in the pseudopolyrotaxane could be transported to the target sites of the Zn anode. The excellent electrolyte presents a high ionic conductivity of 8 mS cm^{-1}, and the Zn//Zn symmetrical cell delivers a cycling lifespan of 1370 h at 0.7 mA cm^{-2}/0.7 mAh cm^{-2}. Eventually, the Zn//MnO_2 full battery using this hydrogel electrolyte demonstrates an excellent capacity retention of 90% for 1000 cycles, which is higher than that of the pure $ZnSO_4$ electrolyte.[204]

A common challenge in polysaccharide-based hydrogel electrolytes lies in the inverse relationship between mechanical strength and ionic conductivity: densely crosslinked networks typically suppress polymer segmental motion and reduce free volume, thereby limiting ion diffusion. To overcome this tradeoff, recent strategies have focused on constructing hierarchical or heterogeneous network architectures that decouple mechanical support from ionic transport. For example, the introduction of sacrificial hydrogen bonds or reversible coordination interactions (*e.g.*, between Zn^{2+} and carboxyl/hydroxyl groups) enables energy dissipation under stress while preserving continuous hydrated channels. Another effective design involves spatially segregated domains, where rigid crystalline regions provide mechanical integrity, and amorphous, highly hydrated domains rich in polar functional groups serve as expressways for Zn^{2+} migration. This microstructure-level compartmentalization, often achieved through phase separation or directional freezing, allows simultaneous achievement of high tensile strength and superior ionic conductivity. Consequently, these well-engineered hydrogel networks not only suppress dendrite penetration but also support rapid, sustained Zn^{2+} flux, as reflected in high Zn^{2+} transference numbers.

4.1.3. Adapting to harsh temperatures. Hydrogel electrolytes face critical challenges in extreme environments, including freezing at low temperatures and dehydration upon heating, which deteriorate their mechanical and electrochemical performance. To overcome these limitations, a polyanionic hydrogel (BBAS) was engineered by incorporating borax-crosslinked bacterial cellulose into a poly(AMPS-*co*-AM) matrix, enabling selective ion transport and robust thermal tolerance (Fig. 4a). The hydrophilic functional groups within the BBAS network effectively inhibit water reactivity and suppress hydrogen evolution. Spectroscopic analysis reveals that the BBAS hydrogel exhibits a decreased content of strong hydrogen bonds and an increased content of medium and weak hydrogen bonds compared to liquid electrolytes, resulting in a significantly depressed freezing point. This unique hydrogen-bonding environment confers enhanced frost resistance and water retention. Electrochemically, the BBAS hydrogel supports prolonged Zn plating/stripping in symmetric cells: over 2000 h at room temperature, 600 h at 50 °C, and 2000 h at −50 °C under 1 mA cm^{-2}/1 mAh cm^{-2} (Fig. 4b and c). When integrated into a Zn–I_2 full battery, it delivers over 6500 stable cycles with a mere 1.9% capacity loss and exhibits no capacity decay even at −50 °C, underscoring its promise for extreme-temperature energy storage applications.[205]

To address the challenge of low-temperature operation in flexible ZIBs, Huang *et al.* designed a dual-network hydrogel electrolyte (CSAM-C) based on $Zn(ClO_4)_2$, PAM, and carboxymethyl chitosan. The anti-freezing property originates from the Hofmeister effect, wherein chaotropic ClO_4^- ions disrupt the hydrogen-bonding network among free water molecules and instead form a ternary hydrogen-bond system with polymer chains and water (Fig. 4d and e). This structural reorganization is evidenced by FTIR spectroscopy, which shows an increased fraction of weak hydrogen bonds (Fig. 4f), and low-field nuclear magnetic resonance (NMR), which confirms the predominance of bound water states (Fig. 4g). The resulting suppression of ice formation enables exceptional low-temperature performance: at −30 °C, the CSAM-C hydrogel maintains an ionic conductivity of 7.8 mS cm^{-1}, supports stable Zn plating/stripping in symmetric cells for 1200 h, and allows a Zn//polyaniline full battery to deliver 70 mAh g^{-1} at 5 A g^{-1} without capacity decay.[206] To overcome transport limitations in hydrogel electrolytes, Zhang *et al.* designed an anisotropic carboxymethyl cellulose (CMC) hydrogel with vertically aligned ion channels *via* directional freezing. The inclusion of $Zn(ClO_4)_2$ establishes a ternary hydrogen-bonding network that depresses the freezing point to −65.3 °C, ensuring low-temperature functionality. The aligned architecture not only provides mechanical robustness (tensile strength: 0.45 MPa) and high ionic conductivity (27.35 mS cm^{-1}) but also fundamentally improves Zn^{2+} transport kinetics. Compared to an isotropic control, the anisotropic hydrogel increases the Zn^{2+} transference number from 0.35 to 0.42, reduces desolvation activation energy from 41.4 to 38.4 kJ mol^{-1}, and elevates exchange current density from 16.97 to 28.38 mA cm^{-2}, while favoring planar Zn^{2+} diffusion. These electrochemical enhancements translate into superior device performance: Zn//Zn symmetric cells cycle stably for over 1200 h at 2 mA cm^{-2}/2 mAh cm^{-2}, Zn//Cu cells sustain 300 h of operation, and Zn//MnO_2 full cells demonstrate excellent cyclability across both ambient and sub-zero (−10 °C) temperatures.[207] The hydrogen bonds also could be regulated by the extra additives. For example, trehalose was introduced into the sodium alginate hydrogel electrolyte to address the pain points in ZIBs. Sodium alginate synergizes with trehalose to enhance the stability of water molecules, thus reducing the freezing possibility at low temperatures. A decent ionic conductivity of 12 mS cm^{-1} can still be retained at −20 °C. Under such a low temperature, the Zn//Zn symmetric cell can work for

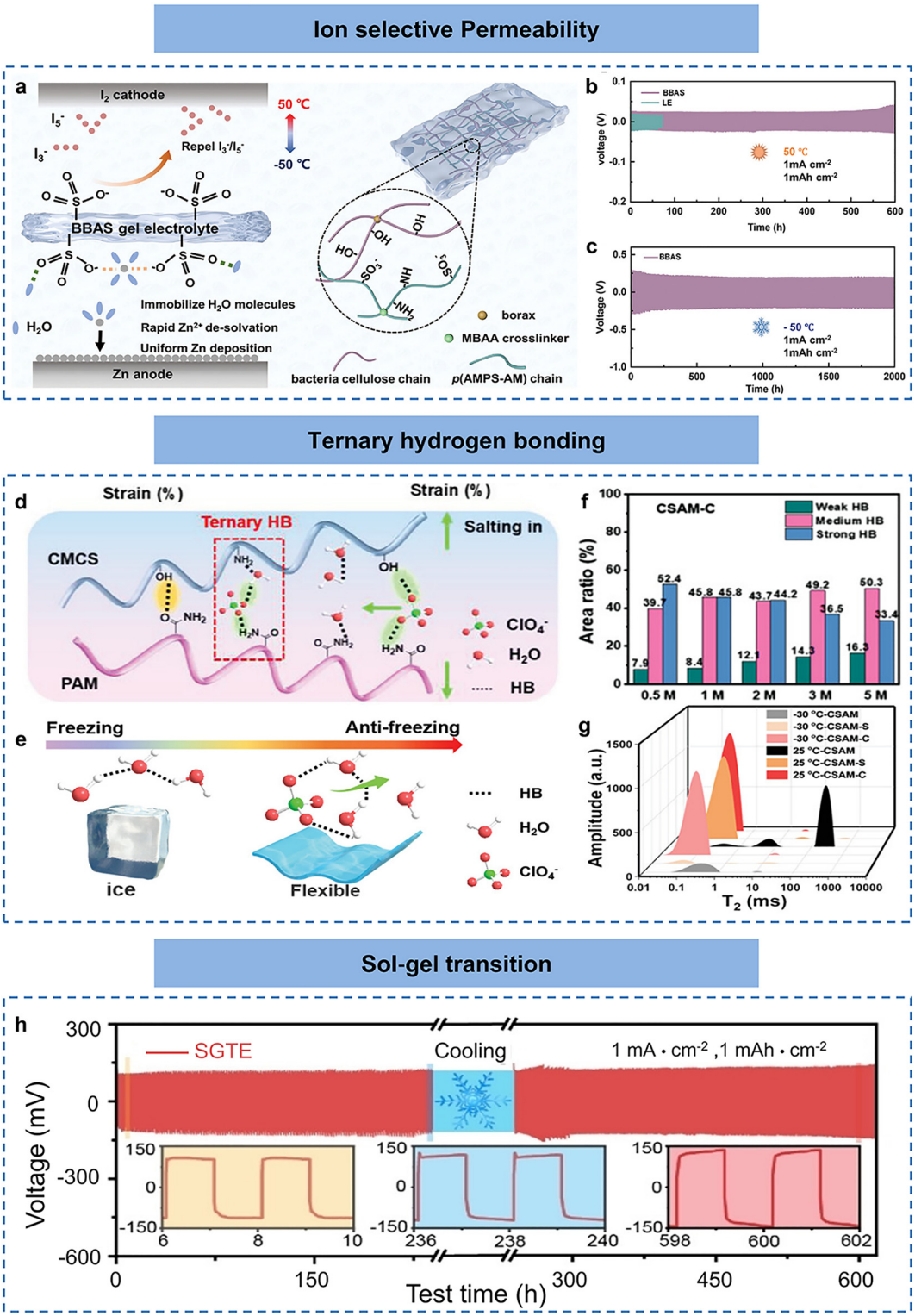

Fig. 4 Methods for adapting to harsh temperatures. (a) Illustration of the work mechanism of the BBAS hydrogel electrolyte. The plating/stripping performance of Zn//Zn cells under (b) 50 °C and (c) −50 °C. Reproduced from ref. 205 with permission from Wiley-VCH, copyright 2024. (d) Schematic diagram of the interactions among CMCS, ClO_4^-, and PAM chains. (e) Schematic illustrations of the anti-freezing mechanism. (f) The area ratio summaries of the strong, medium, and weak hydrogen bonds. (g) Relaxation time distribution curves of low-field NMR for different hydrogels under −30 and 25 C. Reproduced from ref. 206 with permission from Elsevier, copyright 2023. (h) Overpotential variation trend of the Zn//Zn cell using SGTE under different temperatures. Reproduced from ref. 209 with permission from Wiley-VCH, copyright 2023.

200 h at 0.5 mA cm^{-2}/0.25 mAh cm^{-2}, and the Zn//polyaniline full battery demonstrates a capacity retention of 87.0% at 0.2 A g^{-1}.[208] Similarly, a functional three-dimensional network hydrogel (PAM crosslinked with cellulose nanofibers) lined with a hydrogen bond acceptor (dimethylsulfoxide) was designed to guarantee the stable operation of the Zn//MnO_2 full battery at −20 °C.[59]

Flexible ZIBs using hydrogel electrolytes are often vulnerable to irreversible capacity loss due to the fragile electrode–electrolyte interface at a low temperature. Materials with dynamic adaptation mechanisms are desirable. A supramolecular sol–gel transition hydrogel electrolyte (SGTE) comprising α-cyclodextrin and PEO blocks in Pluronic was developed through a host–guest interaction. α-Cyclodextrin with an adequate cavity size of around 4.5 Å can self-assemble with PEO blocks by hydrophobic and non-covalent interactions. Structural stability and thermo-sensitivity could be improved. The obtained electrolyte could be induced to a gel state when the temperature reaches 26 °C, and it would convert to a flowing sol stage upon cooling. This process is highly reversible. Accordingly, the supramolecular hydrogel shows excellent versatility, which could be compatible with several Zn salts, including $ZnSO_4$, $Zn(CF_3SO_3)_2$, and $ZnCl_2$. Such superior gel–sol transition property ensured stable operation of the Zn//Zn symmetric cell for over 600 h when the ambient temperature was changed from room temperature to 0 °C and then back to room temperature (Fig. 4h). This is attributed to the re-infiltration of electrolytes, allowing the electrolyte/electrode interface to be re-compacted.[209]

The anti-freezing capability of polysaccharide-based hydrogel electrolytes primarily originates from the disruption of the intrinsic hydrogen-bonding network of bulk water by polysaccharide chains and their functional groups. In pure water, water molecules form extensive, ordered hydrogen bonds with each other, which readily crystallize into ice at sub-zero temperatures. Upon introduction of polysaccharides or their derivatives, the abundant polar groups on the polymer chains compete to form strong hydrogen bonds with water molecules. This competition breaks the long-range ordered hydrogen-bonding network among water molecules and converts it into a more disordered, short-range hydrogen-bonding configuration. As a result, the freezing point of the confined water is significantly depressed, and ice crystallization is effectively inhibited. Additionally, the incorporation of chaotropic ions (*e.g.*, ClO_4^-) or cryoprotective additives further enhances this effect by forming ternary hydrogen-bonding systems (polymer–water–additive) and increasing the fraction of bound water. Consequently, polysaccharide-based hydrogels maintain high ionic conductivity and stable Zn plating/stripping performance even under sub-zero conditions, enabling reliable operation of flexible ZIBs in cold environments.

4.2. Functions of polysaccharides as electrolyte additives

4.2.1. Reconstructing the solvent sheath. All electrochemical reactions occurring at the Zn anode of ZIBs are intrinsically governed by the physicochemical properties of hydrated Zn^{2+} ions. In conventional aqueous Zn-based electrolytes, Zn^{2+} ions preferentially coordinate with six water molecules to form thermodynamically stable $[Zn(H_2O)_6]^{2+}$ ion pairs. During the plating process, a substantial number of reactive water molecules are present at the Zn anode surface. The dissociation of H_2O into OH^- and H^+ typically leads to the formation of alkaline by-products and hydrogen gas. These side reactions impede ion and electron transport, thereby compromising the reversibility of Zn electrochemistry and promoting Zn dendrite growth. Furthermore, the large ionic radius of hydrated Zn^{2+} ions (5.5 Å) necessitates high energy input to cleave the Zn^{2+}–H_2O bond during deposition. Therefore, modulating the solvation structure of Zn^{2+} ions to suppress dendrite formation and side reactions is essential for stabilizing ion diffusion and electron transfer.[210] Electrolyte engineering based on mixing some additives is of great interest owing to simple preparation and cost-effectiveness. The desolvation and nucleation processes could be adjusted, thus facilitating uniform sedimentation. Among them, polysaccharide materials have been extensively reported as electrolyte additives.

To modulate the solvation structure of Zn^{2+} ions, Huang *et al.* employed sodium carboxymethyl cellulose as an additive in an aqueous $ZnSO_4$ electrolyte, leveraging its abundant polar groups (Fig. 5a). Spectroscopic evidence from NMR and Raman analyses confirms the release of partially bound water from the primary coordination shell and the formation of strong hydrogen bonds between water molecules and carboxymethyl cellulose. MD simulations further reveal that $–COO^-$ groups penetrate the hydration sheath, decreasing the number of coordinated water molecules. Owing to strong adsorption, the additive accumulates predominantly at the electrode/electrolyte interface, thereby concentrating its solvation-structure modulation in this critical region. Such preferential adsorption steers Zn deposition toward the uniform (101) crystallographic plane, effectively mitigating dendrite formation (Fig. 5b). Correspondingly, field emission scanning electron microscopy (FESEM) shows that the addition of carboxymethyl cellulose promotes anisotropic growth of Zn and ensures a more integrated fusion state at nucleation sites (Fig. 5c). Additionally, the limiting current density is elevated compared to that of the pristine $ZnSO_4$ electrolyte, reflecting substantially enhanced hydrodynamic stability. Leveraging these advantages, the modified electrolyte delivers a plating/stripping cycle life of 3700 h at 1 mA cm^{-2} and 0.5 mAh cm^{-2}.[211] Moreover, the chelation effect between chitosan chains and Zn^{2+} ions effectively decouples the pristine $[Zn(H_2O)_6]^{2+}$ solvation structure. This chelation primarily originates from the coordination of transition metal ions with polar functional groups ($–NH_2$ and –OH), which allows chitosan molecules to bind strongly to Zn^{2+} ions and thereby inhibit dendrite formation. Under the optimized electrolyte, the Zn//Zn symmetric cell exhibits a cycling lifespan of 3000 h at 1 mA cm^{-2} and 1 mAh cm^{-2}. Furthermore, the Zn//MnO_2 battery demonstrates excellent long-term stability, retaining 86.79% of its initial capacity after 500 cycles.[212] Duan *et al.* introduced sodium alginate into the $ZnSO_4$ electrolyte, where its carboxyl groups competitively coordinate with Zn^{2+}

ions, displacing water from the primary solvation shell and reducing active water contact with the anode. The polar functional groups of sodium alginate restructure the coordination environment between anions and cations, as reflected by a

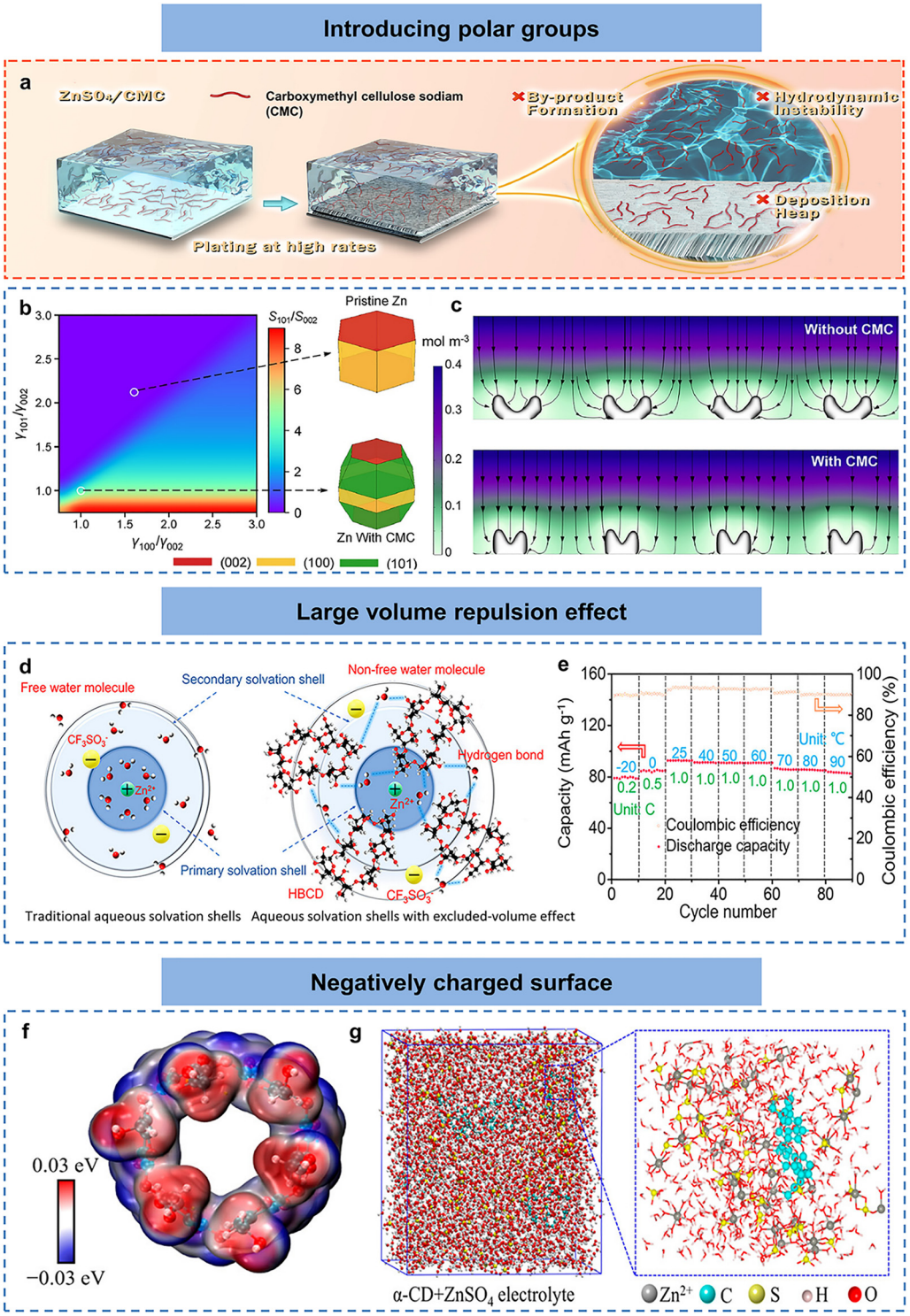

Fig. 5 Methods for reconstructing the solvent sheath. (a) Schematic of the electrochemical reactions at the anode/electrolyte interface stabilized by carboxymethyl cellulose. (b) Contour diagram illustrating the ratio between (101) and (002) facets. (c) FES results demonstrating the anisotropic growth at the nucleation sites. Reproduced from ref. 211 with permission from Elsevier, copyright 2023. (d) Schematic illustration of Zn^{2+} solvation shells in different electrolytes. (e) Temperature-dependent performances of the Zn-organic battery from −20 to 90 °C. Reproduced from ref. 214 with permission from American Chemical Society, copyright 2022. (f) MESP distribution of α-cyclodextrin. (g) 3D snapshot of the α-cyclodextrin-modified $ZnSO_4$ electrolyte based on MD simulation. Reproduced from ref. 51 with permission from American Chemical Society, copyright 2022.

pronounced red shift in the –OH vibrational band, indicative of a reinforced hydrogen-bonding network. Consequently, the HER is effectively suppressed. Strong chelation between the alginate and the Zn anode drives the *in situ* formation of a modified interphase that curtails the random two-dimensional diffusion of Zn^{2+} ions, directing their preferential transport and promoting uniform redistribution during electrodeposition. The optimized electrolyte enables a Zn//Zn symmetric cell to achieve an extended cycling lifespan exceeding 2500 h at 2 mA cm^{-2} and 1 mAh cm^{-2}, while Zn//Na_3VO_4 full cells maintain stable operation over 600 cycles with a specific capacity above 150 mAh g^{-1}.[213] To reshape the primary solvation shell of hydrated Zn^{2+} ions in a $Zn(CF_3SO_3)_2$-based electrolyte, Wei *et al.* utilized (2-hydroxypropyl)-β-cyclodextrin (HBCD), a molecule with a size two orders of magnitude larger than that of water, thereby introducing a distinct excluded-volume effect (Fig. 5d). Linear sweep voltammetry demonstrates that the incorporation of HBCD significantly expands the limiting potentials for both oxygen and hydrogen evolution reactions. Spectroscopic analyses (FTIR, Raman, and ^1H NMR) further confirm that the hydroxyl side groups of HBCD disrupt the original hydrogen-bonding network. Benefiting from these effects, the resulting *N*,*N*′-(2,5-dichloro-1,4-phenylene)diethanesulfonamide-based Zn-organic battery achieves a high open-circuit voltage of 1.7 V and a broad operational temperature range from −20 to 90 °C (Fig. 5e), maintaining 98.3% of its initial capacity after 2000 cycles.[214] In another sample, 10 mM α-cyclodextrin can regulate the solvation structure of Zn^{2+} ions through the exterior surface, where the outer surface is predominantly negatively charged (Fig. 5f). The MD simulation directly verifies that Zn^{2+} ions are mainly around the exterior surface of α-cyclodextrin (Fig. 5g), which acts as a buffered layer to facilitate ion diffusion. The diffusion coefficient calculated from the mean-squared displacement *versus* time increases from 9.70×10^{-7} to 1.18×10^{-6} cm^2 s^{-1} after the addition of α-cyclodextrin. The formulated electrolyte system renders a reversible plating/stripping process (cycling life over 1000 h) in the symmetric cell at 1 mA cm^{-2}/1 mAh cm^{-2}. The Zn//V_2O_5 full battery shows a maximum capacity of around 350 mAh g^{-1} at 0.2 A g^{-1} and an excellent capacity retention of 84.20% for 800 cycles at 3 A g^{-1}.[51] In addition, α-cyclodextrin could offer enough electrons to induce the (002) deposition and redistribute the charge density, thus facilitating a robust Zn anode.[215]

The competitive displacement of water molecules from the primary solvation sheath of Zn^{2+} ions by polysaccharides results from the abundant polar functional groups. These groups exhibit stronger binding affinity to Zn^{2+} ions than water molecules due to their higher electron density and favorable coordination geometry. Specifically, the oxygen atoms of carboxylate ($–COO^-$) or hydroxyl (–OH) groups can donate lone-pair electrons to the empty orbitals of Zn^{2+} ions, forming stable coordinate bonds. Meanwhile, the amino groups ($–NH_2$) in chitosan can engage in both coordination and hydrogen-bonding interactions. Additionally, the extensive hydrogen-bonding network among polysaccharide chains and water molecules disrupts the original hydrogen-bonding environment around hydrated Zn^{2+} ions, further facilitating the release of bound water. As a result, the number of water molecules in the primary solvation sheath is reduced, suppressing water-induced side reactions, while also lowering the desolvation energy barrier for Zn deposition.

4.2.2. Regulating interfacial chemistry. Modulating interfacial chemistry on the Zn anode to affect the deposition process is a promising method. A series of inorganic and organic materials were adopted to construct high-performance interfacial layers. Relatively speaking, organic materials especially polymers with favorable coordination of functional groups could form a crowded interphase to regulate ion distribution and water content. Some polysaccharide materials have specific adsorption to Zn metal and can adapt to the changing electrochemical interface.[216] The crowding environment would induce a Zn-rich and water-poor structure to improve the overall stability.

To cope with the dismal interfacial chemistry, Wu *et al.* put forward a cellulose nanocrystal additive into $ZnSO_4$ solution to construct a self-repairing interphase. Theoretical calculation results evidence that the oxygen-containing groups promote the reconstruction of the solvation structure and decrease the coordinated water molecules, thus enhancing the transport kinetics of Zn^{2+} ions. More critically, the self-assembly characteristics of cellulose nanocrystals together with their inherent electronegativity generate a dynamic interface. The cross-section SEM images (Fig. 6a) depict that the cellulose nanocrystal additive can achieve flat Zn deposition. Further, the *in situ* Raman spectra in Fig. 6b clearly reflect a stable Zn^{2+} flux at the anode/electrolyte interface. The dynamic protective mechanism for the restoration of the impaired interfaces was further evidenced by FES. Correspondingly, the Zn anode can steadily run for 6400 h in a symmetric cell at 1 mA cm^{-2}/1 mAh cm^{-2} and yields an excellent rate performance from 5 to 60 mAh cm^{-2}. The Zn//MnO_2 full battery displays a maximum capacity of 296.3 mAh cm^{-2} at 0.5 A g^{-1} and a high capacity retention of 76.3% for 3000 cycles at 10 A g^{-1}.[42] In addition, Meng *et al.* found that the β-cyclodextrin additive blocked the production of by-products ($Zn_4SO_4(OH)_6{\cdot}xH_2O$) and rendered the high flatness of Zn foil after cycling (Fig. 6c). Besides, the application of β-cyclodextrin can effectively guide the even Zn deposition along the (002) plane as confirmed by confocal laser microscopy (Fig. 6d). A long stable cycling life of 1700 h at 4 mA cm^{-2}/2 mAh cm^{-2} could be achieved. The Zn//V_2O_5 full battery coupled with β-cyclodextrin yields superior cycling stability for 1000 cycles with a small attenuation rate of 0.055 mAh g^{-1} per cycle.[217]

It has been reported that the additives with hydrophobicity not only facilitate the desolvation of Zn^{2+} ions, but also tune the diffusion path and deposition process at the anode/electrolyte interface based on the charge shielding effect. For example, adding sodium carboxymethyl cellulose into the $ZnSO_4$ solution could obtain a colloidal electrolyte. For the pure $ZnSO_4$ electrolyte, the hydrated Zn^{2+} ions could only get to the OHP. In contrast, the sodium carboxymethyl cellulose additive

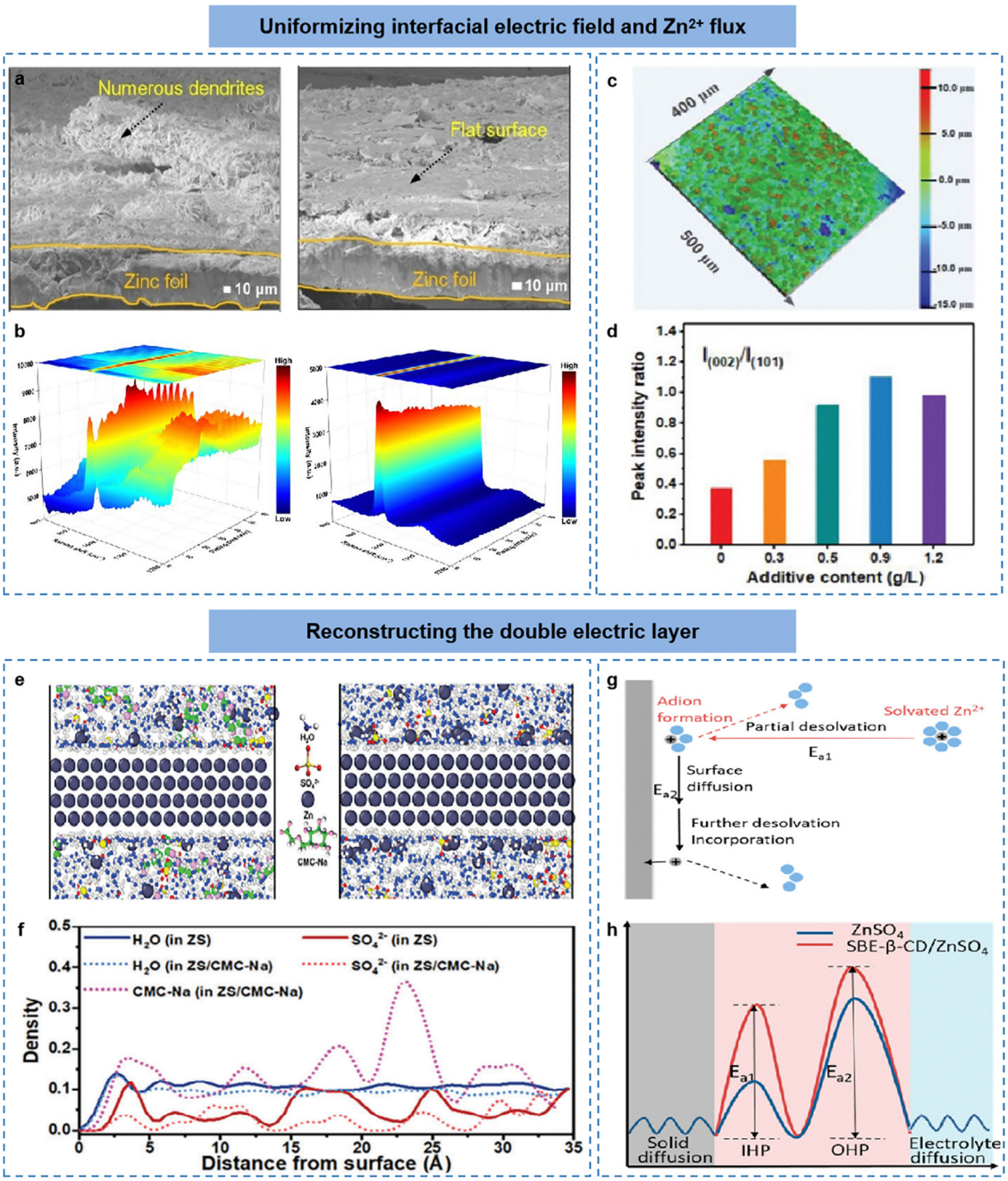

Fig. 6 Methods for regulating interfacial chemistry. (a) Cross-sectional SEM of Zn anodes after 10 cycles in different electrolytes. (b) *In situ* Raman spectra of v-SO_4^{2-} based on symmetrical cells tested in different electrolytes. Reproduced from ref. 42 with permission from Wiley-VCH, copyright 2024. (c) Confocal laser microscopy of the Zn electrode deposited in the β-CD/$ZnSO_4$ electrolyte. (d) $I_{(002)}/I_{(101)}$ ratios of Zn electrodes deposited in electrolytes with different concentrations of β-CD. Reproduced from ref. 212 with permission from Wiley-VCH, copyright 2022. (e) MD simulation snapshot of different electrolytes on Zn anode surfaces. (f) Density distributions of SO_4^{2-}, H_2O, and CMC-Na on the surface of a Zn anode. Reproduced from ref. 218 with permission from Wiley-VCH, copyright 2023. (g) Schematic representation of the electrocrystallization of solvated Zn^{2+} onto the Zn substrate. (h) Correlation of the energy barrier of Zn^{2+} in the IHP and OHP. Reproduced from ref. 220 with permission from American Chemical Society, copyright 2023.

preferentially penetrates into the IHP, leading to a decrease in the density of Zn^{2+} ions. MD simulation results are consistent with the Zn^{2+} density distribution (Fig. 6e), indicating the preferential adsorption of sodium carboxymethyl cellulose. Meanwhile, the density distributions of all components demonstrate that sodium carboxymethyl cellulose reduces the content of SO_4^{2-} anions and water molecules to protect the Zn anode (Fig. 6f). Also, the electrolyte component was *in situ* converted into a SEI layer. The cycling lifespan of the Zn plating/stripping behavior could be prolonged to 2000 h at

5 mA cm^{-2}/5 mAh cm^{-2}.[218] Similarly, Zhao *et al.* proposed carboxymethyl chitosan (CMCS) as a cost-effective zwitterionic electrolyte additive to stabilize Zn anodes. The molecule possesses both NH_3^+ cations and COO^- anions, endowing it with preferential adsorption capability on the Zn anodes. Under the electric field, reversible adsorption occurs at the anode/electrolyte interface, presenting a preferential configuration on the Zn(002) facet and promoting uniform and dendrite-free Zn deposition. Additionally, the adsorption layer formed by CMCS molecules effectively repels water molecules and suppresses side reactions. Experimental results demonstrate that with an optimized concentration of 0.3 g L^{-1} CMCS additive, symmetric Zn//Zn cells exhibit an extended lifespan of 800 h under testing conditions of 1 mA cm^{-2} and 1 mAh cm^{-2}, achieving an average CE of 98.75%.[219] Furthermore, anionic sulfobutyl ether β-cyclodextrin was employed to modify the structure of the EDL at the anode interface (Fig. 6g). The adsorption energies and the differential charge density distribution from DFT calculations indicate that this additive is predominantly adsorbed on the Zn(002) facet. Besides, the potential of zero charges suggests that more negative charges originating from the cyclodextrin anions accumulate on the surface of the Zn anode, which could reduce the electric field gradient, enabling a uniform Zn^{2+} flux. For the regulation of the desolvation process, the activation energy of the charge transfer for penetrating the OHP (from 14.63 kJ mol^{-1} to 34.92 kJ mol^{-1}) and IHP (from 37.16 kJ mol^{-1} to 46.97 kJ mol^{-1}) is increased (Fig. 6h). As a result, the Zn//Zn symmetric cell showcases an ultrahigh cumulative capacity of 10000 mAh cm^{-2} at 10 mA cm^{-2}. The Zn//MnO_2 full battery delivers the largest capacity of 298.9 mAh g^{-1} at 0.3 A g^{-1} and achieves a capacity retention of 78.1% at 1 A g^{-1} for 3000 cycles.[220] In addition, the addition of α-cyclodextrin into the $ZnSO_4$ electrolyte solution also affects the deposition process of Zn^{2+} ions. The controllable epitaxial Zn (002) plane growth could be successfully achieved. Eventually, the cycling stability of the Zn//Zn symmetric cell and the assembled Zn//MnO_2 battery in the electrolyte containing α-cyclodextrin is strikingly improved.[221]

5. Conclusion and perspectives

This review compiles the recent advances in natural polysaccharide-based electrolytes for ZIBs. As the additives and main components of hydrogels, polysaccharides have drawn paramount attention in the optimization of electrolytes due to some vital properties, including eco-friendliness, abundant polar groups, high mechanical strength, and stable structures. Hence, the chemical constitution, applied destination, and electrochemical properties of polysaccharides as hydrogel components (Table 1) and additives (Table 2) are systematically summarized. From the application point of view, multifunctional additives and hydrogels made of polysaccharides are two main directions to enhance the electrochemical performance of ZIBs.

The superior mechanical properties and toughness of hydrogels stem from a chemical composition abundant in polar groups and hydrogen-bonding sites, which underpin a high Young's modulus and structural stability. For example, cotton is converted into cellulose to form a polymer framework, followed by the introduction of tetraethyl orthosilicate and glycerol. The resulting Si–O–Si linkages, combined with extensive hydrogen bonding, confer both high tensile strength and elasticity. Additionally, strategies such as physical entanglement, solvent replacement, and the salting-out effect further enhance the fatigue resistance and mechanical robustness of polysaccharide-based hydrogels.

As a momentous component in ZIBs, the electrolyte is associated with many critical parameters in batteries, including ionic conductivity, rate performance, high/low-temperature stress tolerance, flexibility, and electrolyte/electrode interfacial stability (Scheme 3). Polysaccharides and their derivatives were used to construct a 3D framework with covalent and hydrogen-bonding interactions to homogenize Zn^{2+} flux, thereby improving ionic conductivity. Furthermore, there are a large number of negatively charged functional groups in polysaccharides that can serve as jump migration sites to accelerate the migration of Zn^{2+} ions. Pure Zn salts as the electrolytes of traditional cells are usually fragile under subzero conditions. In contrast, the numerous hydrogen bonds between polysaccharides and water molecules benefit the water retention ability, and the corresponding electrochemical performances are well maintained under harsh conditions. In addition, it is promising to apply polysaccharide-based quasi-solid hydrogels as electrolytes to improve the overall mechanical properties, increase the ionic conductivity, and extend the operating temperature range, ultimately leading to long cycle life and practical application possibilities. Moreover, polysaccharides can also be used as electrolyte additives to participate in the solvent sheath structure of hydrated Zn^{2+} ions through electrostatic interaction, chelation, and volume exclusion effects, thus inhibiting the decomposition of water molecules and the occurrence of side reactions. Furthermore, the adsorption energies of most polysaccharide additives to the Zn slab are greater than that of the pure H_2O molecule. Generally, the additives are enriched at the electrolyte/electrode interfaces, reducing the contents of water molecules and anion ions. The electric and Zn^{2+} concentration fields are thereby homogenized accompanying the accelerated desolvation process during the electroplating process.

However, more effort is required to stimulate further research and commercialization of polysaccharide-based electrolytes. Based on the above analyses, some challenges and potential development directions are coming up, eagerly anticipating the broader application of polysaccharide-based electrolytes beyond the laboratory scale. For the emerging polysaccharide-based electrolyte, there are various strategies mentioned above to modify the polysaccharide materials or combine them with other substances for the excellent performance of ZIBs. At present, there is little research on the deep mechanisms that improve the electrochemical performances of polysaccharides. For example, the reasons for applying polar groups in the hydrogel electrolytes as the migration sites of Zn^{2+} ions should be explained. The specific functional

Table 1 Various polysaccharide-based hydrogels for aqueous ZIBs

No.	Materials	Mechanical properties	Ionic conductivity	Temperature adaptation	Cyclic stability	Ref.
1	Cellulose/TEOS/glycerol	Fracture strain/stress of 846%/2.11 MPa	38.5, 19.4 mS cm^{-1} (60, −40 °C)	−40 to 60 °C	800 h (2 mA cm^{-2}, 2 mAh cm^{-2})	40
2	Carboxymethylcellulose/rigid cellulose/NaOH	Fracture strain/stress of 48%/72 ± 5 MPa	26 mS cm^{-1}	8 to 25 °C	350 cycles (10 mA cm^{-2}, 5 mAh cm^{-2})	168
3	Chitosan/PAM/$Zn(ClO_4)_2$	Fracture strain/stress of 1200%/50 kPa	31.6 mS cm^{-1}	Room temperature	1500 h (10 mA cm^{-2}, 10 mAh cm^{-2})	45
4	Chitosan/PAM/PAA/MXene	Fracture strain/stress of 800%/1.8 MPa	22 mS cm^{-1}	Room temperature	700 h (0.5 mA cm^{-2}, 0.5 mAh cm^{-2})	169
5	PVA/SA/boric acid/glycerol	Fracture strain/stress of 559.1%/869.4 kPa	16.18 S cm^{-1}	Room temperature	—	171
6	SA/PAM/SBMA	Fracture strain/stress of 310.2%/61.8 kPa	25 mS cm^{-1}	−20 to 20 °C	380 h (1 mA cm^{-2}, 1 mAh cm^{-2})	63
7	SA/glycerol	—	32.8 mS cm^{-1}	Room temperature	600 h (2 mA cm^{-2}, 2 mAh cm^{-2})	172
8	STA	Fracture strain/stress of 75%/3.5 MPa	22.85 mS cm^{-1}	Room temperature	3000 h (1 mA cm^{-2}, 1 mAh cm^{-2})	128
9	PVA/Zn acetate/Zn alginate	Fracture strain/stress of 145%/4 MPa	16.5 mS cm^{-1}	Room temperature	1450 h (1 mA cm^{-2}, 1 mAh cm^{-2})	174
10	Chitosan/PAM	Fracture strain/stress of 2670%/80 kPa	11.6 mS cm^{-1}	Room temperature	370 h (0.5 mA cm^{-2}, 0.5 mAh cm^{-2})	175
11	PAM/SA/KI	Fracture strain/stress of 550%/15 kPa	82 mS cm^{-1}	Room temperature	110 h (1 mA cm^{-2})	177
12	Chitosan/kappa(*k*)-carrageenan	Fracture strain/stress of 45%/14.2 MPa	5.3 mS cm^{-1}	25 °C	4000 h (10 mA cm^{-2}, 35 mAh cm^{-2})	178
13	SA/PAZ	Fracture strain/stress of 49%/3.04 MPa	24.01 mS cm^{-1}	Room temperature	1050 h (1 mA cm^{-2}, 1 mAh cm^{-2})	179
14	Gelatin/chitosan/β-cyclodextrin	Fracture strain/stress of 400%/1.49 MPa	24.89 mS cm^{-1}	Room temperature	1200 h (1 mA cm^{-2}, 1 mAh cm^{-2})	166
15	Cellulose/Zn	Fracture strain/stress of 145%/2.08 MPa	38.6 mS cm^{-1}	Room temperature	400 h (10 mA cm^{-2}, 10 mAh cm^{-2})	180
16	Cellulose/NaOH/urea/H_2O/ECH	Fracture strain/stress of 80%/2.18 MPa	24.1 mS cm^{-1}	Room temperature	800 h (5 mA cm^{-2}, 5 mAh cm^{-2})	181
17	Cellulose nanofibers/DMAc/LiCl	Fracture strain/stress of 128%/3.22 MPa	26.2 mS cm^{-1}	Room temperature	2400 h (1 mA cm^{-2}, 1 mAh cm^{-2})	182
18	Carboxylethyl quaternized cellulose/PAM	Fracture strain/stress of 990%/200 kPa	27.5 mS cm^{-1}	Room temperature	700 h (20 mA cm^{-2}, 20 mAh cm^{-2})	184
19	PAM/carboxymethyl cellulose/agarose	Fracture strain/stress of 121.4%/5.6 MPa	38.78 mS cm^{-1}	Room temperature	2500 h (1 mA cm^{-2}, 1 mAh cm^{-2})	185
20	PVA/cellulose nanofibers/graphene oxide	—	16.18 mS cm^{-1}	Room temperature	2200 h (1 mA cm^{-2}, 1 mAh cm^{-2})	186
21	Carboxylate cellulose/xanthan gum	Fracture strain/stress of 5%/60 MPa	0.117 mS cm^{-1}	Room temperature	3600 h (0.5 mA cm^{-2}, 0.5 mAh cm^{-2})	187
22	Protonated chitosan/Zn-chitosan	—	0.0024 mS cm^{-1}	Room temperature	1200 h (10 mA cm^{-2}, 1 mAh cm^{-2})	188
23	Chitosan/Zn-MOF-74/acetic acid	Fracture strain/stress of 50%/120 kPa	18.2 mS cm^{-1}	Room temperature	—	189
24	Sulfonated chitosan/PAM	Fracture strain/stress of 155%/54.2 kPa	38.1 mS cm^{-1}	Room temperature	2600 h (1 mA cm^{-2}, 1 mAh cm^{-2})	190
25	SA/chitosan	—	—	Room temperature	6500 h (1 mA cm^{-2}, 1 mAh cm^{-2})	48
26	Chlorophyll derivative/chitosan/glycidyl methacrylate	Fracture strain/stress of 9%/14.9 MPa	3.6 mS cm^{-1}	Room temperature	1700 h (0.5 mA cm^{-2}, 0.5 mAh cm^{-2})	191
27	MXene/chitosan/acetic acid	—	1.61 mS cm^{-1}	Room temperature	2200 h (1 mA cm^{-2}, 1 mAh cm^{-2})	192
28	Chitosan/NaOH	Fracture stress of 7.4 MPa	72 mS cm^{-1}	Room temperature	1000 cycles (50 mA cm^{-2}, 10 mAh cm^{-2})	193
29	SA	Fracture strain/stress of 163.4%/4.63 MPa	0.54 mS cm^{-1}	Room temperature	2200 h (2mA cm^{-2}, 0.5 mAh cm^{-2})	61
30	SA/H_2SO_4	Fracture strain/stress of 23%/5 MPa	11.3 mS cm^{-1}	Room temperature	1724 h (2 mA cm^{-2}, 1 mAh cm^{-2})	195
31	Zinc alginate/thermoplastic polyurethane	Fracture strain/stress of 450%/3.2 MPa	16.4 mS cm^{-1}	Room temperature	1200 h (5 mA cm^{-2}, 5 mAh cm^{-2})	196
32	SA/poly(3,4-ethylenedioxythiophene):polystyrene sulfonate	Fracture strain/stress of 300%/270 kPa	41 mS cm^{-1}	Room temperature	6750 h (1 mA cm^{-2}, 1 mAh cm^{-2})	197
33	SA/tannic acid	—	24.2 mS cm^{-1}	Room temperature	300 h (1.13 mA cm^{-2})	199
34	SA/vermiculite sheets	—	4.52 mS cm^{-1}	Room temperature	1000 h (2 mA cm^{-2}, 1 mAh cm^{-2})	202

Table 1 (*continued*)

No.	Materials	Mechanical properties	Ionic conductivity	Temperature adaptation	Cyclic stability	Ref.
35	PAM/polyethylene oxide/α-cyclodextrins	Fracture strain/stress of 778%/273.3 kPa	22.4 mS cm^{-1}	Room temperature	160 h (1 mA cm^{-2})	203
36	Chitosan/β-cyclodextrin	Fracture strain/stress of 218.9%/96.5 kPa	24.89 mS cm^{-1}	Room temperature	1200 h (1 mA cm^{-2}, 1 mAh cm^{-2})	166
37	Borax-bacterial cellulose/p(AMPS-AM)	Fracture strain/stress of 140%/55.8 kPa	37.6 mS cm^{-1}	−50 to 50 °C	2000 h (1 mA cm^{-2}, 1 mAh cm^{-2})	205
38	$Zn(ClO_4)_2$/PAM/carboxymethyl chitosan	Fracture strain/stress of 620%/0.35 MPa	7.8 mS cm^{-1} (−30 °C)	−30 °C to room temperature	1200 h (0.5 mA cm^{-2}, 0.5 mAh cm^{-2}, −30 °C)	206
39	CMC/H_2SO_4/$Zn(ClO_4)_2$	Fracture strain/stress of 17.5%/0.45 MPa	27.35 mS cm^{-1}	−10 °C to room temperature	1200 h (2 mA cm^{-2}, 2 mAh cm^{-2})	207
40	Trehalose/SA	Fracture stress of 186.6 kPa	12 mS cm^{-1} (−20 °C)	−20 °C to room temperature	200 h (0.5 mA cm^{-2}, 0.25 mAh cm^{-2}, −30 °C)	208
41	DMSO/PAM/cellulose nanofibers	Fracture strain/stress of 1126%/55.4 kPa	1.52 mS cm^{-1} (−30 °C)	−30 °C to room temperature	1300 h (2 mA cm^{-2}, 2 mAh cm^{-2})	61
42	α-Cyclodextrin/PEO/Pluronic	—	58.3 mS cm^{-1} (30 °C)	0 °C to 30 °C	600 h (1 mA cm^{-2}, 1 mAh cm^{-2})	209

Table 2 Various polysaccharide-based additives for aqueous ZIBs

No.	Materials	Ionic conductivity (mS cm^{-1})	Zn^{2+} transference number	Cyclic stability	Ref.
1	Sodium carboxymethyl cellulose	20.7	—	3700 h (1 mA cm^{-2}, 0.5 mAh cm^{-2})	211
2	Chitosan	60.3	0.37	3000 h (1 mA cm^{-2}, 1 mAh cm^{-2})	212
3	Sodium alginate	14.3	0.625	2500 h (2 mA cm^{-2}, 1 mAh cm^{-2})	213
4	(2-Hydroxypropyl)-β-cyclodextrin	24.4	—	300 h (5 mA cm^{-2}, 5 mAh cm^{-2})	214
5	Carboxymethyl chitosan	0.121	0.67	2400 h (0.5 mA cm^{-2}, 0.5 mAh cm^{-2})	216
6	Cellulose nanocrystal	15.3	—	6400 h (1 mA cm^{-2}, 1 mAh cm^{-2})	42
7	β-Cyclodextrin	54	—	1700 h (4 mA cm^{-2}, 2 mAh cm^{-2})	217
8	Carboxymethyl cellulose	52	0.443	2000 h (5 mA cm^{-2}, 5 mAh cm^{-2})	218
9	Carboxymethyl chitosan	30.15	0.588	800 h (1 mA cm^{-2}, 1 mAh cm^{-2})	219
10	Sulfobutylether-β-cyclodextrin	51.5	—	2000 h (10 mA cm^{-2}, 10 mAh cm^{-2})	220
11	α-Cyclodextrin	55.3	—	770 h (6 mA cm^{-2}, 6 mAh cm^{-2})	221

components of the SEI formed by the polysaccharides during the charging/discharging processes should be revealed. For the limited understanding of SEI composition, employing advanced surface-sensitive techniques such as time-of-flight secondary ion mass spectrometry (TOF-SIMS) and X-ray photoelectron spectroscopy (XPS) with depth profiling is essential to identify the specific functional groups from polysaccharides that participate in SEI formation during charge/discharge cycling.

To thoroughly investigate the underlying mechanism, a combination of *in situ* and *ex situ* characterization techniques, such as energy-dispersive X-ray spectroscopy (EDS), X-ray diffraction (XRD), and Raman spectroscopy, can be employed to elucidate the material composition. More advanced and high-resolution characterization methods, including cryo-SEM and cryo-STEM, are essential for probing ionic transport and interfacial evolution in various electrolyte systems. To address the lack of *in situ* characterization, cryo-SEM and cryo-STEM protocols also could be adopted to directly visualize Zn dendrite suppression by polysaccharide hydrogels and additives under realistic current densities (*e.g.*, 5–10 mA cm^{-2}), combined with *operando* optical microscopy to track dynamic interfacial evolution. Regarding the poor recycling and sustainability of polysaccharide materials, we suggest designing closed-loop recycling processes for spent polysaccharide-based electrolytes, including dissolution-regeneration of hydrogel networks or recovery of polysaccharide additives *via* filtration and re-crosslinking, while assessing the retained electrochemical performance over multiple reuse cycles. In addition, the highly quantitative and nondestructive analysis of quasi-solid-state electrolytes under varying temperatures or external stresses relies on commonly used spectroscopic techniques such as FTIR and Raman. For complex electrolyte systems that are difficult to probe experimentally, theoretical calculations, MD simulations, and FES also prove extremely valuable.

A major technical bottleneck remains in the construction of *in situ* analytical devices that combine electrochemical measurement platforms with stress application or temperature modulation systems. There is currently a pronounced disparity between laboratory testing conditions and practical application scenarios. For instance, the use of commercially available Zn foil as anodes provides an excessive Zn supply, with utilization

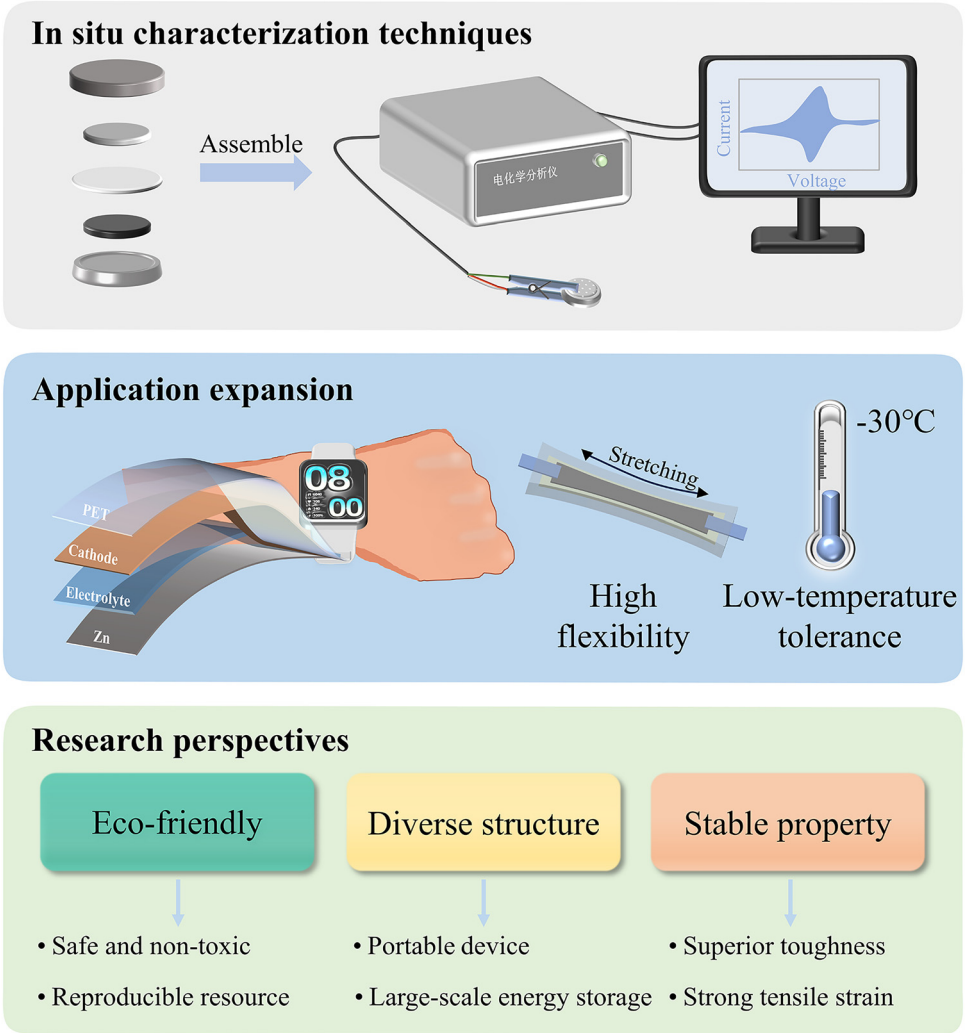

Scheme 3 Summary and prospects of polysaccharide-containing electrolytes toward future flexible aqueous energy storage devices.

rates often in the single digits. When the Zn content is reduced and the DOD is increased, the capacity performance of ZIBs degrades rapidly. Furthermore, excess Zn compromises energy density, hindering the ability to meet market requirements. For the issue of low Zn utilization, future studies could be systematically performed to evaluate polysaccharide-based electrolytes under practical conditions using thin Zn foils (*e.g.*, 10–30 μm) and high DOD (>50%) in pouch cell formats, while consistently reporting Zn mass loading alongside cycling parameters. As a result, many research findings remain confined to the laboratory and cannot be effectively translated into productivity. To better reflect real-world performance, key electrochemical parameters, such as cycle life and power density, should be evaluated under high DOD conditions and in pouch-type battery formats.

Beyond electrochemical performance, the commercial viability of polysaccharide-based electrolytes also depends on the extraction costs and scalability of the raw materials. Cellulose, as the most abundant biopolymer on earth, can be cost-effectively derived from wood pulp, cotton, or agricultural residues, using established industrial processes such as the kraft or sulfite pulping methods. Chitosan, while slightly more expensive due to the deacetylation of chitin from crustacean shells, benefits from the utilization of seafood industry waste, making it both economical and environmentally beneficial. Alginates, extracted from brown seaweed, are produced at moderate costs through simple alkaline extraction, and their gelling properties are already exploited in food and pharmaceutical industries at large scales. Cyclodextrins, produced *via* enzymatic degradation of starch, are more expensive but have found applications in drug delivery and food additives, suggesting feasibility for high-value energy storage applications. Nevertheless, further cost reduction strategies, such as optimizing extraction conditions, utilizing underutilized biomass sources, and developing continuous production processes, are needed to compete with synthetic polymers. Future research should also consider the economic trade-offs between performance gains and material costs to guide the selection of appropriate polysaccharides for specific ZIB applications.

To date, the application of polysaccharides in aqueous ZIBs is mainly concentrated in quasi-solid hydrogel electrolytes and electrolyte additives, and there are few studies on polysaccharide-based electrodes, separators, and binders. Therefore, it is even rare to integrate multiple polysaccharide-based battery devices to explore the compatibility and the interaction between components of polysaccharides. Also, in many studies, the recycling of polysaccharide materials in batteries after failure has not been paid enough attention. However, given the great potential of future development of polysaccharides, it can be expected that there will be more and more research into environmentally friendly, structurally diverse, and stable polysaccharides that will be able to meet people's demand for energy storage devices while achieving green environmental protection.

Author contributions

Yi Kong and Yong Hu designed the scope of the manuscript. Bin-Bin Xie, Hongfei Wang, and Yi Kong wrote the manuscript. Jiele Chen and Hangyi Shen discussed the manuscript. Jicheng Li revised the manuscript. All authors approved the final version.

Conflicts of interest

There are no conflicts to declare.

Data availability

No primary research results, software or code have been included and no new data were generated or analyzed as part of this review.

Acknowledgements

The authors appreciate the financial support by the National Natural Science Foundation of China (22272150 and 22502176), the Zhejiang Provincial Natural Science Foundation of China (LMS26B030007 and LZ23B030001), the National College Students Innovation and Entrepreneurship Training Program (202410345027), the Open Project of State Key Laboratory of Synergistic Chem-Bio Synthesis (sklscbs202517), and the Key Science and Technology Project of Jinhua City (2023-1-093).

References

1 J.-Y. Hwang, S.-T. Myung and Y.-K. Sun, *Chem. Soc. Rev.*, 2017, **46**, 3529–3614.
2 Y. Guo, J. Bae, Z. Fang, P. Li, F. Zhao and G. Yu, *Chem. Rev.*, 2020, **120**, 7642–7707.
3 V. V. Tyagi, S. C. Kaushik, S. K. Tyagi and T. Akiyama, *Renew. Sust. Energy Rev.*, 2011, **15**, 1373–1391.
4 H.-M. Zeng, X.-J. Wang, Z.-G. Jiang and C.-H. Zhan, *Inorg. Chem. Front.*, 2024, **11**, 1207–1213.
5 W. Y. Du, Y. H. Zhang, H. Duan, Y. K. Lv, Z. Y. Song, L. H. Gan and M. X. Liu, *Sci. Adv.*, 2026, **12**, eaec9924.
6 P. X. Liu, Z. Y. Song, Q. Huang, Z. F. Xu, Y. K. Lv, L. H. Gan and M. X. Liu, *Angew. Chem., Int. Ed.*, 2026, **65**, e25690.
7 Y. M. Chen, D. Zhang, Y. Qin, C. M. Hu, L. Miao, Y. K. Lv, Z. Y. Song, L. H. Gan and M. X. Liu, *Nat. Commun.*, 2026, **17**, 3599.
8 D. Lin, Y. Liu and Y. Cui, *Nat. Nanotechnol.*, 2017, **12**, 194–206.
9 R. Reinhardt, I. Christodoulou, S. Gassó-Domingo and B. Amante García, *J. Environ. Manage.*, 2019, **245**, 432–446.
10 P. Simon and Y. Gogotsi, *Nat. Mater.*, 2008, **7**, 845–854.
11 J. B. Goodenough and Y. Kim, *Chem. Mater.*, 2009, **22**, 587–603.
12 B. He, J. Song, H. Li, Y. Li, Y. Tang, Z. Su and Q. Hao, *Vacuum*, 2022, **205**, 111386.
13 H. Wang, W. Ye, B. Yin, K. Wang, M. S. Riaz, B. B. Xie, Y. Zhong and Y. Hu, *Angew. Chem., Int. Ed.*, 2023, **62**, e202218872.
14 C. Tian, J. Wang, R. Sun, T. Ali, H. Wang, B. B. Xie, Y. Zhong and Y. Hu, *Angew. Chem., Int. Ed.*, 2023, **62**, e202310970.
15 C. Tian, H. Wang, L. Xie, Y. Zhong and Y. Hu, *Adv. Energy Mater.*, 2024, **14**, 2400276.
16 Y. An, Y. Tian, C. Liu, S. Xiong, J. Feng and Y. Qian, *ACS Nano*, 2021, **15**, 15259–15273.
17 Y. Zhao, P. Zhang, J. Liang, X. Xia, L. Ren, L. Song, W. Liu and X. Sun, *Energy Storage Mater.*, 2022, **47**, 424–433.
18 M. Liao, J. Wang, L. Ye, H. Sun, Y. Wen, C. Wang, X. Sun, B. Wang and H. Peng, *Angew. Chem., Int. Ed.*, 2019, **59**, 2273–2278.
19 D. Gupta, S. Liu, R. Zhang and Z. Guo, *Adv. Energy Mater.*, 2025, **15**, 2500171.
20 A. Ali, J. Mohammadi Moradian, A. Naveed, S. Zhang, M. H. Tahir, K. Shehzad and M. Sillanpää, *Prog. Mater. Sci.*, 2026, **156**, 101543.
21 F. Dong, Y. Li, Q. Zhang, Z. Wang, Z. Ni, Y. Li, B. Xi, S. Xiong, X. Tian and J. Feng, *Prog. Mater. Sci.*, 2026, **159**, 101652.
22 Y. He, Y. Liu, W. Shang, Q. Ma, J. Wei and P. Tan, *Electrochem. Energy Rev.*, 2026, **9**, 1.
23 Y. Chen, B. Yin, Y. Zeng, H. Wang, B.-B. Xie, D. Luan, Y. Hu and X. W. Lou, *Chem*, 2025, **11**, 102411.
24 Y. Wang, Y. Kong, T. Zhang, C. Chen, H. Wang and Y. Hu, *Adv. Energy Mater.*, 2025, **15**, 2502353.
25 F. Wang, O. Borodin, T. Gao, X. Fan, W. Sun, F. Han, A. Faraone, J. A. Dura, K. Xu and C. Wang, *Nat. Mater.*, 2018, **17**, 543–549.
26 H. Pan, Y. Shao, P. Yan, Y. Cheng, K. S. Han, Z. Nie, C. Wang, J. Yang, X. Li, P. Bhattacharya, K. T. Mueller and J. Liu, *Nat. Energy*, 2016, **1**, 16039.
27 Q. Meng, T. Yan, Y. Wang, X. Lu, H. Zhou and S. Dong, *Chem. Eng. J.*, 2024, **497**, 154541.
28 H. Yousefzadeh, A. Noori, M. S. Rahmanifar, N. Hassani, M. Neek-Amal, M. F. El-Kady, A. Vinu, R. B. Kaner and M. F. Mousavi, *Adv. Energy Mater.*, 2023, **13**, 2302137.
29 B. He, P. Zhao, G.-X. Pan, Q. Lu, H.-Q. Li, F. Ye, Y.-W. Tang, Q.-L. Hao and Z. Su, *J. Alloys Compd.*, 2023, **938**, 168673.
30 W. Jia, Q. Lu, W. Zheng, K. Wang, X. Liu, S. Yang and B. He, *Nanoscale Adv.*, 2023, **5**, 4133–4139.
31 J. Hao, B. Li, X. Li, X. Zeng, S. Zhang, F. Yang, S. Liu, D. Li, C. Wu and Z. Guo, *Adv. Mater.*, 2020, **32**, 2003021.
32 L. E. Blanc, D. Kundu and L. F. Nazar, *Joule*, 2020, **4**, 771–799.
33 X. Liu, L. Sun, Z. Zhao and Q. Lu, *J. Energy Storage*, 2024, **89**, 111822.
34 A. Toleuova, D. Kurmangaliyeva, D. Batyrbekuly, K. Maratova, N. Umirov, A. Dauletbay, S.-T. Myung, Z. Bakenov and A. Konarov, *J. Power Sources*, 2025, **658**, 238454.
35 H. Li, S. Li, R. Hou, Y. Rao, S. Guo, Z. Chang and H. Zhou, *Chem. Soc. Rev.*, 2024, **53**, 7742–7783.
36 Y. Zeng, X. Zhang, Y. Meng, M. Yu, J. Yi, Y. Wu, X. Lu and Y. Tong, *Adv. Mater.*, 2017, **29**, 1700274.
37 H. Dong, J. Li, J. Guo, F. Lai, F. Zhao, Y. Jiao, D. J. L. Brett, T. Liu, G. He and I. P. Parkin, *Adv. Mater.*, 2021, **33**, 2007548.
38 J. Li, A. Azizi, S. Zhou, S. Liu, C. Han, Z. Chang, A. Pan and G. Cao, *eScience*, 2025, **5**, 100294.
39 X. He, L. Zhao, Y. Zhang, X. Zhang, J. Yi and Q. Xu, *Adv. Funct. Mater.*, 2025, **35**, e10796.
40 M. Chen, J. Chen, W. Zhou, X. Han, Y. Yao and C. P. Wong, *Adv. Mater.*, 2021, **33**, 2007559.
41 G. Shi, X. Peng, J. Zeng, L. Zhong, Y. Sun, W. Yang, Y. L. Zhong, Y. Zhu, R. Zou, S. Admassie, Z. Liu, C. Liu, E. I. Iwuoha and J. Lu, *Adv. Mater.*, 2023, **35**, 2300109.
42 Q. Wu, J. Huang, J. Zhang, S. Yang, Y. Li, F. Luo, Y. You, Y. Li, H. Xie and Y. Chen, *Angew. Chem., Int. Ed.*, 2024, **63**, e202319051.

43 J. Gao, S. Zhang, C. Jiang, F. Bai, J. Yan, W. Liu, C. Lin and M. Liu, *Adv. Energy Mater.*, 2026, **16**, e06462.
44 A. Lang, Z. Liang, W. Yang, Z. Guo, K. Ocakoglu, E. Iwuoha, R. Xia and X. Peng, *J. Bioresour. Bioprod.*, 2026, **11**, 100232.
45 Q. Liu, Z. Yu, Q. Zhuang, J. K. Kim, F. Kang and B. Zhang, *Adv. Mater.*, 2023, **35**, 2300498.
46 M. B. Arif, D. Annas, E. Yulianti, Q. Sabrina, Sudaryanto, E. Triwulandari, W. K. Restu, S. T. C. L. Ndruru and M. Ghozali, *J. Power Sources*, 2025, **660**, 238502.
47 H. Dong, X. Hu, R. Liu, M. Ouyang, H. He, T. Wang, X. Gao, Y. Dai, W. Zhang, Y. Liu, Y. Zhou, D. J. L. Brett, I. P. Parkin, P. R. Shearing and G. He, *Angew. Chem., Int. Ed.*, 2023, **62**, e202311268.
48 X. Cai, X. Wang, Z. Bie, Z. Jiao, Y. Li, W. Yan, H. J. Fan and W. Song, *Adv. Mater.*, 2023, **36**, 2306734.
49 S. Tian, Y. Ding, Z. Tian, S. Zhang, F. Li, F. Shi and J. Mei, *J. Power Sources*, 2026, **667**, 239272.
50 Y. Zhang, Y. Sun, K. Liu, Q. Xia, S. Zhao, Q. Ying, P. Chen, H. Lu, T. Shahid, X. Peng, Z. Ye and Y. Yang, *Adv. Funct. Mater.*, 2026, **36**, e20280.
51 K. Zhao, G. Fan, J. Liu, F. Liu, J. Li, X. Zhou, Y. Ni, M. Yu, Y.-M. Zhang, H. Su, Q. Liu and F. Cheng, *J. Am. Chem. Soc.*, 2022, **144**, 11129–11137.
52 K. Wang, T.-T. Su, C.-Y. Shao, W.-F. Ren and R.-C. Sun, *ACS Sustain. Chem. Eng.*, 2022, **10**, 16225–16237.
53 S. J. Zhang, J. Hao, H. Li, P. F. Zhang, Z. W. Yin, Y. Y. Li, B. Zhang, Z. Lin and S. Z. Qiao, *Adv. Mater.*, 2022, **34**, 2201716.
54 J. Jia, D. Han, H. G. Gerken, Y. Li, M. Sommerfeld, Q. Hu and J. Xu, *Algal Res.*, 2015, **7**, 66–77.
55 N. Mittal, A. Ojanguren, D. Kundu, E. Lizundia and M. Niederberger, *Small*, 2022, **19**, 2206249.
56 M. Nishio, Y. Umezawa, J. Fantini, M. S. Weiss and P. Chakrabarti, *Phys. Chem. Chem. Phys.*, 2014, **16**, 12648–12683.
57 P. Sun, W. Liu, D. Yang, Y. Zhang, W. Xiong, S. Li, J. Chen, J. Tian and L. Zhang, *Electrochim. Acta*, 2022, **429**, 140985.
58 J.-H. Park, S. Hyun Park, D. Joung and C. Kim, *Chem. Eng. J.*, 2022, **433**, 133532.
59 S. Huang, S. He, Y. Li, S. Wang and X. Hou, *Chem. Eng. J.*, 2023, **464**, 142607.
60 W. Zhu, Z. Lei and P. Wu, *Energy Environ. Sci.*, 2025, **18**, 3647–3658.
61 L. Hong, X. Wu, Y. S. Liu, C. Yu, Y. Liu, K. Sun, C. Shen, W. Huang, Y. Zhou, J. S. Chen and K. X. Wang, *Adv. Funct. Mater.*, 2023, **33**, 2300952.
62 M. Zhang, J.-H. Li, Y. Tang, D.-W. Wang, H. Hu, M. Liu, B. Xiao and P.-F. Wang, *Energy Storage Mater.*, 2024, **65**, 103113.
63 T. Wu, C. Ji, H. Mi, F. Guo, G. Guo, B. Zhang and M. Wu, *J. Mater. Chem. A*, 2022, **10**, 25701–25713.
64 X. Fan, R. Zhang, S. Sui, X. Liu, J. Liu, C. Shi, N. Zhao, C. Zhong and W. Hu, *Angew. Chem., Int. Ed.*, 2023, **62**, e202302640.
65 D. Zhao, Q. Zhu, Q. Zhou, W. Zhang, Y. Yu, S. Chen and Z. Ren, *Energy Environ. Mater.*, 2023, **7**, e12522.
66 W. Guo, T. Hua, C. Qiao, Y. Zou, Y. Wang and J. Sun, *Energy Storage Mater.*, 2024, **66**, 103244.
67 J. W. Li, A. Azizi, S. Zhou, S. N. Liu, C. Han, Z. Chang, A. Q. Pan and G. Z. Cao, *Escience*, 2025, **5**, 100294.
68 R. J. Jia, C. L. Wei, B. X. Ma, L. H. Li, C. H. Yang, B. B. Wang, L. W. Tan and J. K. Feng, *Adv. Funct. Mater.*, 2025, **35**, 2417498.
69 J. Hao, X. Li, X. Zeng, D. Li, J. Mao and Z. Guo, *Energy Environ. Sci.*, 2020, **13**, 3917–3949.
70 J. Zhong, C. Xia, T. Zhang, H. Wang, H. Tao, C. Lian and Y. Hu, *Adv. Funct. Mater.*, 2026, **36**, e27894.
71 C. Xu, B. Li, H. Du and F. Kang, *Angew. Chem., Int. Ed.*, 2011, **51**, 933–935.
72 F. Yang, L. Zhou, T. Zhang, H. Wang, C. Xia, Z. Ma and Y. Hu, *Angew. Chem., Int. Ed.*, 2026, **65**, e23653.
73 Q. Ma, A. Ma, S. Lv, B. Qin, Y. Xu, X. Zeng, W. Ling, Y. Liu and X. Wu, *J. Energy Chem.*, 2024, **93**, 609–626.
74 T. Wu, C. Hu, Q. Zhang, Z. Yang, G. Jin, Y. Li, Y. Tang, H. Li and H. Wang, *Adv. Funct. Mater.*, 2024, **34**, 2315716.
75 M. Zhao, Y. Lv, J. Qi, Y. Zhang, Y. Du, Q. Yang, Y. Xu, J. Qiu, J. Lu and S. Chen, *Adv. Mater.*, 2024, **36**, 2412667.
76 X. Xie, S. Liang, J. Gao, S. Guo, J. Guo, C. Wang, G. Xu, X. Wu, G. Chen, J. J. E. Zhou and E. Science, *Energy Environ. Sci.*, 2020, **13**, 503–510.
77 J. X. Zheng and L. A. Archer, *Sci. Adv.*, 2021, **7**, eabe0219.
78 P. Bai and M. Z. Bazant, *Nat. Commun.*, 2014, **5**, 3585.
79 M. Yan, C. Xu, Y. Sun, H. Pan and H. Li, *Nano Energy*, 2021, **82**, 105739.
80 J. Xiao, *Science*, 2019, **366**, 426–427.
81 Z. Cao, P. Zhuang, X. Zhang, M. Ye, J. Shen and P. M. Ajayan, *Adv. Energy Mater.*, 2020, **10**, 2001599.
82 J. Liu, C. Li, Q. Lv, D. Chen, J. Zhao, X. Xia, Z. Wu, J. Lai and L. Wang, *Adv. Energy Mater.*, 2024, **14**, 2401118.
83 Y.-Y. Hsieh and H.-Y. Tuan, *Energy Storage Mater.*, 2024, **68**, 103361.
84 E. Emanuele, G. Batignani, G. Cerullo, G. Leita, N. M. Mohanan, E. Mai, M. Martinati, C. Mele, T. Scopigno and B. Bozzini, *J. Mater. Chem. A*, 2025, **13**, 9778–9790.
85 Y. Marcus, *Chem. Rev.*, 2009, **109**, 1346–1370.
86 N. Zhang, F. Cheng, Y. Liu, Q. Zhao, K. Lei, C. Chen, X. Liu and J. Chen, *J. Am. Chem. Soc.*, 2016, **138**, 12894–12901.
87 J. Wang, Y. Yang, Y. Zhang, Y. Li, R. Sun, Z. Wang and H. Wang, *Energy Storage Mater.*, 2021, **35**, 19–46.
88 T. Zhang, Y. Tang, S. Guo, X. Cao, A. Pan, G. Fang, J. Zhou and S. Liang, *Energy Environ. Sci.*, 2020, **13**, 4625–4665.
89 M. S. Ding, L. Ma, M. A. Schroeder and K. Xu, *J. Phys. Chem. C*, 2020, **124**, 25249–25253.
90 M. S. Ding, A. von Cresce and K. Xu, *J. Phys. Chem. C*, 2017, **121**, 2149–2153.
91 L. Wang, Y. Zhang, H. Hu, H.-Y. Shi, Y. Song, D. Guo, X.-X. Liu and X. Sun, *ACS Appl. Mater. Interface*, 2019, **11**, 42000–42005.
92 D. Li, L. Cao, T. Deng, S. Liu and C. Wang, *Angew. Chem., Int. Ed.*, 2021, **60**, 13035–13041.
93 C. Yan, H.-R. Li, X. Chen, X.-Q. Zhang, X.-B. Cheng, R. Xu, J.-Q. Huang and Q. Zhang, *J. Am. Chem. Soc.*, 2019, **141**, 9422–9429.
94 X. Guo, Z. Zhang, J. Li, N. Luo, G.-L. Chai, T. S. Miller, F. Lai, P. Shearing, D. J. L. Brett, D. Han, Z. Weng, G. He and I. P. Parkin, *ACS Energy Lett.*, 2021, **6**, 395–403.
95 C. Zhang, J. Holoubek, X. Wu, A. Daniyar, L. Zhu, C. Chen, D. P. Leonard, I. A. Rodríguez-Pérez, J.-X. Jiang, C. Fang and X. Ji, *Chem. Commun.*, 2018, **54**, 14097–14099.
96 W. Yang, X. Du, J. Zhao, Z. Chen, J. Li, J. Xie, Y. Zhang, Z. Cui, Q. Kong, Z. Zhao, C. Wang, Q. Zhang and G. Cui, *Joule*, 2020, **4**, 1557–1574.
97 T. Sun, X. Yuan, K. Wang, S. Zheng, J. Shi, Q. Zhang, W. Cai, J. Liang and Z. Tao, *J. Mater. Chem. A*, 2021, **9**, 7042–7047.
98 A. Moezzi, M. Cortie and A. M. McDonagh, *Eur. J. Inorg. Chem.*, 2013, 1326–1335.
99 L. M. Suo, O. Borodin, T. Gao, M. Olguin, J. Ho, X. L. Fan, C. Luo, C. S. Wang and K. Xu, *Science*, 2015, **350**, 938–943.
100 X. Nie, Y. Yang, J. Hu, D. Yuan, L. Hu and L.-F. Chen, *J. Mater. Chem. A*, 2025, **13**, 41443–41461.
101 Z. Wang, L. Bai, H. Fan, Y. Wang and W. Liu, *J. Energy Chem.*, 2024, **94**, 740–757.
102 G. Li, Z. Liu, Q. Huang, Y. Gao, M. Regula, D. Wang, L.-Q. Chen and D. Wang, *Nat. Energy*, 2018, **3**, 1076–1083.
103 J. Luan, Q. Zhang, H. Yuan, D. Sun, Z. Peng, Y. Tang, X. Ji and H. Wang, *Adv. Sci.*, 2019, **6**, 1901433.
104 A. Mitha, A. Z. Yazdi, M. Ahmed and P. Chen, *ChemElectroChem*, 2018, **5**, 2409–2418.
105 C. Zhao, L. Liu, Y. Lu, M. Wagemaker, L. Chen and Y. S. Hu, *Angew. Chem., Int. Ed.*, 2019, **58**, 17026–17032.
106 Q. Yang, G. Liang, Y. Guo, Z. Liu, B. Yan, D. Wang, Z. Huang, X. Li, J. Fan and C. Zhi, *Adv. Mater.*, 2019, **31**, 1903778.
107 R. Zhang, X. R. Chen, X. Chen, X. B. Cheng, X. Q. Zhang, C. Yan and Q. Zhang, *Angew. Chem., Int. Ed.*, 2017, **56**, 7764–7768.
108 J. Zhao, S. Ma, Z. Wang, Q. Gao, H. Xiao, J. Gao, F. Li and G. Li, *Adv. Funct. Mater.*, 2024, **34**, 2405656.
109 W. D. Zhang, H. L. L. Zhuang, L. Fan, L. N. Gao and Y. Y. Lu, *Sci. Adv.*, 2018, **4**, eaar4410.
110 X.-B. Cheng, R. Zhang, C.-Z. Zhao and Q. J. C. R. Zhang, *Chem. Rev.*, 2017, **117**, 10403–10473.
111 Y. Zuo, K. Wang, P. Pei, M. Wei, X. Liu, Y. Xiao and P. Zhang, *Mater. Today Energy*, 2021, **20**, 100692.
112 X. Zhang, L. Zhang, X. Jia, W. Song and Y. Liu, *Nano-Micro Lett.*, 2024, **16**, 75.
113 G. Chang, S. Liu, Y. Fu, X. Hao, W. Jin, X. Ji and J. Hu, *Adv. Mater. Interfaces*, 2019, **6**, 1901358.
114 X. Zhang, J. P. Hu, N. Fu, W. B. Zhou, B. Liu, Q. Deng and X. W. Wu, *InfoMat*, 2022, **4**, e12306.

115 L. Ma, S. Chen, N. Li, Z. Liu, Z. Tang, J. A. Zapien, S. Chen, J. Fan and C. Zhi, *Adv. Mater.*, 2020, **32**, 1908121.
116 X. Lv, W. Wei, H. Wang, B. Huang and Y. Dai, *Appl. Catal., B*, 2020, **264**, 118521.
117 J. Zhao, J. Zhang, W. Yang, B. Chen, Z. Zhao, H. Qiu, S. Dong, X. Zhou, G. Cui and L. Chen, *Nano Energy*, 2019, **57**, 625–634.
118 Q. B. Zhang, Y. X. Hua, T. G. Dong and D. G. Zhou, *J. Appl. Electrochem.*, 2009, **39**, 1207–1216.
119 F. Duan, S. Jin, Y. Cheng, F. Yang, M. Wei, M. Wang, X. Zhang, Y. Yu, X. Yin, K. Zhao, Y. Wei, L. Wu and Y. Wang, *Nano Lett.*, 2022, **23**, 42–50.
120 A. Bayaguud, Y. Fu and C. Zhu, *J. Energy Chem.*, 2022, **64**, 246–262.
121 K. Zhao, C. Wang, Y. Yu, M. Yan, Q. Wei, P. He, Y. Dong, Z. Zhang, X. Wang and L. Mai, *Adv. Mater. Interfaces*, 2018, **5**, 1800848.
122 J. Zhu, Z.-C. Wang, H. Dai, Q. Wang, R. Yang, H. Yu, M. Liao, J. Zhang, W. Chen, Z. Wei, N. Li, L. Du, D. Shi, W. Wang, L. Zhang, Y. Jiang and G. Zhang, *Nat. Commun.*, 2019, **10**, 1348.
123 C. Li, X. Xie, S. Liang and J. Zhou, *Energy Environ. Mater.*, 2020, **3**, 146–159.
124 J. Hao, X. Li, S. Zhang, F. Yang, X. Zeng, S. Zhang, G. Bo, C. Wang and Z. Guo, *Adv. Funct. Mater.*, 2020, **30**, 2001263.
125 G. Fang, J. Zhou, A. Pan and S. J. A. E. L. Liang, *ACS Energy Lett.*, 2018, **3**, 2480–2501.
126 M. Zhu, J. Hu, Q. Lu, H. Dong, D. D. Karnaushenko, C. Becker, D. Karnaushenko, Y. Li, H. Tang, Z. Qu, J. Ge and O. G. Schmidt, *Adv. Mater.*, 2021, **33**, 2007497.
127 Y. Habibi, L. A. Lucia and O. J. Rojas, *Chem. Rev.*, 2010, **110**, 3479–3500.
128 F. Chen, X. Li, S. P. Chen, Y. Zhang, H. D. Huang, H. Yang, S. Zhou and Z. M. Li, *Adv. Sci.*, 2025, **12**, e11759.
129 H. Zhang, K. Chen, Q. Xu, H. Xie and J. Zhou, *Acc. Mater. Res.*, 2025, **6**, 1232–1245.
130 W. Chen, Q. Li, Y. Wang, X. Yi, J. Zeng, H. Yu, Y. Liu and J. Li, *ChemSusChem*, 2014, **7**, 154–161.
131 H. Qin, K. Fu, Y. Zhang, Y. Ye, M. Song, Y. Kuang, S.-H. Jang, F. Jiang and L. Cui, *Energy Storage Mater.*, 2020, **28**, 293–299.
132 H. Xie, C. Yang, K. Fu, Y. Yao, F. Jiang, E. Hitz, B. Liu, S. Wang and L. Hu, *Adv. Energy Mater.*, 2018, **8**, 1703474.
133 L. Chen, J. Y. Zhu, C. Baez, P. Kitin and T. Elder, *Green Chem.*, 2016, **18**, 3835–3843.
134 W. Yang, J. Liang, Y. Ding, H. Bian, J. Han and H. Dai, *Ind. Crop. Prod.*, 2023, **193**, 116215.
135 H. Nawaz, A. He, Z. Wu, X. Wang, Y. Jiang, A. Ullah, F. Xu and F. Xie, *Int. J. Biol. Macromol.*, 2024, **273**, 133012.
136 S. Zhu, Y. Wu, Q. Chen, Z. Yu, C. Wang, S. Jin, Y. Ding and G. Wu, *Green Chem.*, 2006, **8**, 325.
137 L. Bai, L. Liu, M. Esquivel, B. L. Tardy, S. Huan, X. Niu, S. Liu, G. Yang, Y. Fan and O. J. Rojas, *Chem. Rev.*, 2022, **122**, 11604–11674.
138 A. Ghosh and Y. H. Lee, *ChemSusChem*, 2012, **5**, 480–499.
139 M. Gao, H. Tang and H. Zhu, *Compr. Rev. Food Sci. Food Saf.*, 2024, **23**, e70008.
140 O. Ghorbel-Bellaaj, I. Younes, H. Maâlej, S. Hajji and M. Nasri, *Int. J. Biol. Macromol.*, 2012, **51**, 1196–1201.
141 M. M. Islam, M. Shahruzzaman, S. Biswas, M. Nurus Sakib and T. U. Rashid, *Bioact. Mater.*, 2020, **5**, 164–183.
142 M. M. Rahman, S. Kabir, T. U. Rashid, B. Nesa, R. Nasrin, P. Haque and M. A. Khan, *Radiat. Phys. Chem.*, 2013, **82**, 112–118.
143 J. L. Arias and M. S. Fernández, *Chem. Rev.*, 2008, **108**, 4475–4482.
144 C. Pacheco, F. Sousa and B. Sarmento, *React. Funct. Polym.*, 2020, **146**, 104430.
145 L. S. Cao, D. Li, E. Y. Hu, J. J. Xu, T. Deng, L. Ma, Y. Wang, X. Q. Yang and C. S. Wang, *J. Am. Chem. Soc.*, 2020, **142**, 21404–21409.
146 C. Wang, T. Yokota and T. Someya, *Chem. Rev.*, 2021, **121**, 2109–2146.
147 H. Hecht and S. Srebnik, *Biomacromolecules*, 2016, **17**, 2160–2167.
148 T. Pan, X. Wang, J. Zhu and H. Wang, *Carbohyd. Polym.*, 2024, **337**, 122169.
149 S. N. Pawar and K. J. Edgar, *Biomaterials*, 2012, **33**, 3279–3305.
150 Q. Zhang, J. Y. Luan, L. Fu, S. G. Wu, Y. G. Tang, X. B. Ji and H. Y. Wang, *Angew. Chem., Int. Ed.*, 2019, **58**, 15841–15847.
151 A. de Nigris, G. Quero, G. P. Vanoli and L. Ambrosone, *Appl. Surf. Sci. Adv.*, 2025, **27**, 100739.
152 M. S. Shamsudin, S. F. Azha, L. Sellaoui, M. Badawi, A. Bonilla-Petriciolet and S. Ismail, *Chem. Eng. J.*, 2022, **428**, 131929.
153 S. Tang, J. Yang, L. Lin, K. Peng, Y. Chen, S. Jin and W. Yao, *Chem. Eng. J.*, 2020, **393**, 124728.
154 X. Zhao, X. Wang and T. Lou, *J. Hazard. Mater.*, 2021, **403**, 124054.
155 Y. Feng, H. Wang, J. Xu, X. Du, X. Cheng, Z. Du and H. Wang, *J. Hazard. Mater.*, 2021, **416**, 125777.
156 S. Yadav, D. K. Verma, R. Tiwari, D. Kumar, K. Parwati, R. Rai, P. Adhikary and S. Krishnamoorthi, *Energy Technol.*, 2025, **13**, 2401912.
157 T. J. Kim, Y. D. Lee and H. S. Kim, *Biotechnol. Bioeng.*, 2004, **41**, 88–94.
158 Z. Bai, H. Zhang, R. Xue, X. Lu, X. Li, W. MacSwain, W. Zheng, J. Xu, Y. Yu and Y. L. Bai, *Aggregate*, 2024, **5**, e583.
159 S. Ozturk, B. Balaban, İ. Avcı, T. Tugsuz, M. Atakay and B. Salih, *Food Chem.*, 2025, **492**, 145622.
160 Y. Liu, T. Lin, C. Cheng, Q. Wang, S. Lin, C. Liu and X. Han, *Molecules*, 2021, **26**, 1090.
161 N. Kelanne, B. Yang and O. Laaksonen, *Food Innov. Adv.*, 2024, **3**, 1–10.
162 H. Liu, S. Guo, S. Wei, J. Liu and B. Tian, *Carbohyd. Polym.*, 2024, **329**, 121763.
163 P.-L. Champagne, D. Ester, D. Polan, V. E. Williams, V. Thangadurai and C.-C. Ling, *J. Am. Chem. Soc.*, 2019, **141**, 9217–9224.
164 Y. Su, X. Wang, M. Zhang, H. Guo, H. Sun, G. Huang, D. Liu and G. Zhu, *Angew. Chem., Int. Ed.*, 2023, **62**, e202308182.
165 M. Yu, J. Mu, L. Wang, Y. Niu, W. Si, J. Li, X. Liu, T. Li, X. Li, W. Zheng, Y. Dai, X. Jiang and G. He, *Energy Environ. Sci.*, 2025, **18**, 1502–1513.
166 W. Cai, X. Zhang, G. Li and L. Chen, *Chem. Eng. J.*, 2024, **484**, 149390.
167 Z. Zhang, Y. Mu, L. Xiao, H. Hu, T. Xue, L. Zang, E. Sakai, M. Han, C. Yang, L. Zeng and J. Qiu, *Nano-Micro Lett.*, 2026, **18**, 139.
168 L. Xu, T. Meng, X. Zheng, T. Li, A. H. Brozena, Y. Mao, Q. Zhang, B. C. Clifford, J. Rao and L. Hu, *Adv. Funct. Mater.*, 2023, **33**, 2302098.
169 J. Pu, Y. Gao, Z. Geng, Y. Zhang, Q. Cao, J. Yang, X. Zhao, Y. Wang, J. Wang and C. Guan, *Adv. Funct. Mater.*, 2024, **34**, 2304453.
170 N. Almenara, R. Gueret, A. J. Huertas-Alonso, U. T. Veettil, M. H. Sipponen and E. Lizundia, *ACS Sustain. Chem. Eng.*, 2023, **11**, 2283–2294.
171 C. Yang, C. Ji, F. Guo, C. Jin, H. Mi and Z. Wang, *Nano Res.*, 2023, **17**, 321–332.
172 W. Shang, J. Zhu, Y. Liu, L. Kang, S. Liu, B. Huang, J. Song, X. Li, F. Jiang, W. Du, Y. Gao and H. Luo, *ACS Appl. Mater. Interface*, 2021, **13**, 24756–24764.
173 X. Xie, J. Li, Z. Xing, B. Lu, S. Liang and J. Zhou, *Natl. Sci. Rev.*, 2023, **10**, nwac281.
174 C. Li, W. Wang, J. Luo, W. Zhuang, J. Zhou, S. Liu, L. Lin, W. Gong, G. Hong, Z. Shao, J. Du, Q. Zhang and Y. Yao, *Adv. Mater.*, 2024, **36**, 2313772.
175 Y. Liu, A. Gao, J. Hao, X. Li, J. Ling, F. Yi, Q. Li and D. Shu, *Chem. Eng. J.*, 2023, **452**, 139605.
176 Y. Du, F. Mo, C. Qin, D. Ho and H. Hu, *J. Mater. Chem. A*, 2023, **11**, 18135–18145.
177 Q. Liu, C. Xia, C. He, W. Guo, Z. P. Wu, Z. Li, Q. Zhao and B. Y. Xia, *Angew. Chem., Int. Ed.*, 2022, **61**, e202210567.
178 F. Wang, J. Zhang, H. Lu, H. Zhu, Z. Chen, L. Wang, J. Yu, C. You, W. Li, J. Song, Z. Weng, C. Yang and Q.-H. Yang, *Nat. Commun.*, 2023, **14**, 4211.
179 J. Chen, R. Yang, Y. Chen, D. Liu, S. Meng, W. Liu, F. Wu, W. Shi and X. Cao, *Chem. Commun.*, 2025, **61**, 11685–11688.
180 H. Zhang, X. Gan, Y. Yan and J. Zhou, *Nano-Micro Lett.*, 2024, **16**, 106.
181 W. Yang, J. Zeng, W. Yang, A. Lang, M. Zhao, L. Zhong, J. Lu and X. Peng, *Adv. Funct. Mater.*, 2025, **36**, e07159.
182 F. Cao, B. Wu, T. Li, S. Sun, Y. Jiao and P. Wu, *Nano Res.*, 2021, **15**, 2030–2039.
183 D. Wang, H. Li, Z. Liu, Z. Tang, G. Liang, F. Mo, Q. Yang, L. Ma and C. Zhi, *Small*, 2018, **14**, 1803978.
184 H. Zhang, X. Gan, Z. Song and J. Zhou, *Angew. Chem., Int. Ed.*, 2023, **62**, e202217833.

185 Y. Wang, K. Ding, X. Gong, S. Chen, A. Sun, J. Zhang and B. Wang, *Chinese Chem. Lett.*, 2026, **37**, 111078.
186 Q. Wang, J. Huang, L. Qi, M. Li, S. Wang, J. Chen, Z. Sui, T. Bi, Q. Tang, L. Yu, P. Hu, W. Zhang, C. Lu and C. Chen, *ACS Nano*, 2025, **19**, 26770–26781.
187 W. B. Tu, S. Liang, L. N. Song, X. X. Wang, G. J. Ji and J. J. Xu, *Adv. Funct. Mater.*, 2024, **34**, 2316137.
188 Z. Zhang, X. Wang, J. Ke, W. Du, Z. Lv, Y. Tang, M. Ye, Y. Zhang, X. Liu, Y. Yang, Z. Wen and C. C. Li, *Adv. Funct. Mater.*, 2024, **34**, 2313150.
189 M. García-Castrillo, S. Dutta, J. Beitia, E. Goikolea, S. K. Ravi, S. Wuttke, I. R. de Larramendi and E. Lizundia, *Carbohyd. Polym.*, 2026, **373**, 124624.
190 Y. Hu, Z. Wang, Y. Li, P. Liu, X. Liu, G. Liang, D. Zhang, X. Fan, Z. Lu and W. Wang, *Chem. Eng. J.*, 2024, **479**, 147762.
191 Y. T. Xu, S. J. Dai, M. J. Gong, J. Z. Zhang, H. Xu, A. Li, S. I. Sasaki, X. X. Zeng, X. W. Wu and X. F. Wang, *Small*, 2023, **20**, 2304463.
192 L. Tan, C. Wei, Y. Zhang, Y. An, S. Xiong and J. Feng, *Chem. Eng. J.*, 2022, **431**, 134277.
193 M. Wu, Y. Zhang, L. Xu, C. Yang, M. Hong, M. Cui, B. C. Clifford, S. He, S. Jing, Y. Yao and L. Hu, *Matter*, 2022, **5**, 3402–3416.
194 R. Yi, X. Shi, Y. Tang, Y. Yang, P. Zhou, B. Lu and J. Zhou, *Small Struct.*, 2023, **4**, 2300020.
195 L. Yan, Q. Zhang, Z. Zhang, G.-J. Li, Y. Jin, X.-L. Zhang and Y.-Y. Sun, *J. Membrane Sci.*, 2024, **690**, 122243.
196 Q. Liu, Y. Wang, X. Hong, R. Zhou, Z. Hou and B. Zhang, *Adv. Energy Mater.*, 2022, **12**, 2200318.
197 D. Wang, D. Zhao, L. Chang, Y. Zhang, W. Wang, W. Zhang and Q. Zhu, *Energy Storage Mater.*, 2025, **74**, 103903.
198 Y. Yang, H. Hua, Z. Lv, M. Zhang, C. Liu, Z. Wen, H. Xie, W. He, J. Zhao and C. C. Li, *Adv. Funct. Mater.*, 2022, **33**, 2212446.
199 B. Zhang, L. Qin, Y. Fang, Y. Chai, X. Xie, B. Lu, S. Liang and J. Zhou, *Sci. Bull.*, 2022, **67**, 955–962.
200 S. Lin, M. Li, G. Wang, C. Wang, H. Yang, Z. Wang, Y. Zhang, X. Liu, J. Bae and Y. Wu, *Small*, 2024, **20**, 2311510.
201 K. Zhao, G. L. Fan, J. D. Liu, F. M. Liu, J. H. Li, X. Z. Zhou, Y. X. Ni, M. Yu, Y. M. Zhang, H. Su, Q. H. Liu and F. Y. Cheng, *J. Am. Chem. Soc.*, 2022, **144**, 11129–11137.
202 L. Pan, H. He, Z. Liu and P. Hu, *J. Power Sources*, 2022, **551**, 232173.
203 H. Xia, G. Xu, X. Cao, C. Miao, H. Zhang, P. Chen, Y. Zhou, W. Zhang and Z. Sun, *Adv. Mater.*, 2023, **35**, 2301996.
204 K. Wu, S. Zhan, W. Liu, X. Liu, F. Ning, Y. Liu, J. Zhang and J. Yi, *ACS Appl. Mater. Interface*, 2023, **15**, 6839–6847.
205 Y. Liu, F. Li, J. Hao, H. Li, S. Zhang, J. Mao, T. Zhou, R. Wang, L. Zhang and C. Zhang, *Adv. Funct. Mater.*, 2024, **34**, 2400517.
206 S. Huang, L. Hou, T. Li, Y. Jiao and P. Wu, *Adv. Mater.*, 2022, **34**, 2110140.
207 Y. Zhang, M. Chen, J. Lu, H. Ma, W. Liu, J. Yu, Q. Tian, J. Xu and J. Chen, *Chem. Eng. J.*, 2025, **506**, 159950.
208 Q. Bai, Q. Meng, W. Liu, W. Lin, P. Yi, J. Tang, G. Zhang, P. Cao and J. Yang, *J. Mater. Chem. A*, 2024, **12**, 277–285.
209 P. Li, M. Liao, S. Cui, J. Li, L. Ye, Y. Yang, C. Wang, B. Wang and H. Peng, *Angew. Chem., Int. Ed.*, 2023, **62**, e202300705.
210 J. Cao, D. Zhang, X. Zhang, Z. Zeng, J. Qin and Y. Huang, *Energy Environ. Sci.*, 2022, **15**, 499–528.
211 H. Huang, J. Yun, H. Feng, T. Tian, J. Xu, D. Li, X. Xia, Z. Yang and W. Zhang, *Energy Storage Mater.*, 2023, **55**, 857–866.
212 T. Li, W. Meng, C. Fan, D. Zuo, S. Deng, D. Li and L. Jiang, *Chem. Eng. J.*, 2024, **484**, 149206.
213 C. Duan, H. Lu, D. Zhang, Z. Zhu, Y. Qin, X. Yuan and Y. Jin, *Chem. Eng. J.*, 2024, **487**, 150413.
214 J. Wei, P. Zhang, T. Shen, Y. Liu, T. Dai, Z. Tie and Z. Jin, *ACS Energy Lett.*, 2022, **8**, 762–771.
215 J. Yang, B. Yin, S. Zhang, Y. Sun, J. Li, D. Su and T. Ma, *Small*, 2023, **19**, 2304913.
216 Z. Hu, X. Wang, W. Du, Z. Zhang, Y. Tang, M. Ye, Y. Zhang, X. Liu, Z. Wen and C. C. Li, *ACS Nano*, 2023, **17**, 23207–23219.
217 C. Meng, W. He, L. Jiang, Y. Huang, J. Zhang, H. Liu and J. J. Wang, *Adv. Funct. Mater.*, 2022, **32**, 2207732.
218 X. Fang, C. Hu, X. Sun, H. Wang and J. Li, *Adv. Energy Mater.*, 2023, **14**, 2302499.
219 K. Zhao, S. Ma, J. Zhao, H. Li, C. Ma, J. Sheng, J. Ding, H. Wang, H. Luo, S. Wu, S. Wang and S. Fang, *J. Colloid Interf. Sci.*, 2026, **702**, 138847.
220 L. Wang, C. Shen, C. Huang, J. Chen and J. Zheng, *ACS Nano*, 2023, **17**, 24619–24631.
221 G. Wang, Q. Dou, P. Xiong, Q. Liu, D. Min and H. S. Park, *Chem. Eng. J.*, 2023, **457**, 141250.

